Theoretical and Experimental Study of the Effects of Cobalt and Nickel Doping within IrO2 on the Acidic Oxygen Evolution Reaction

Luis E. Camacho-Forero,^{1,#} Fernando Godínez-Salomón,^{2,#} Guadalupe Ramos-Sánchez,¹ Christopher P. Rhodes,^{2,*} and Perla B. Balbuena^{1,*}

¹Department of Chemical Engineering, Texas A&M University, College Station, TX 77843,
United States

²Department of Chemistry and Biochemistry, Texas State University, San Marcos, TX 78666, United States

*e-mails: balbuena@tamu.edu, cprhodes@txstate.edu

*These authors contributed equally to this work.

Abstract

The effect of Ni and Co doping within IrO₂ on the structure and oxygen evolution reaction (OER) was studied using integrated theory and experiments. Density Functional Theory (DFT) calculations show that the metal dopant influences the distribution of electronic charge and affects the thermodynamics and kinetics aspects of the OER when compared with undoped IrO₂. Using DFT, multiple different reaction pathways were evaluated for O-O bond formation, and analysis supports the associative mechanism to be the most likely reaction pathway. Calculations showed lower activation energies for Ni and Co-doped IrO₂ compared to undoped IrO₂, in agreement with experimental analysis of the activation energy and OER activity. From experiments, Co-doping shows significantly improved stability compared to Nidoping. Evaluation of the rate-determining step (rds) from calculations and experimental analysis shows apparent differences that indicate the additional factors need to be considered to enable improved correlation between theory and experiment regarding the OER rds.

Keywords: density functional theory, water oxidation, oxygen evolution, doped oxides, reaction mechanisms, activity, stability, Tafel slopes

1. Introduction

Electrolysis of water using renewable electric power, e.g. solar or wind energy, is one of the goals of humanity: an immeasurable source of energy transformed into a very benign chemical product such as hydrogen. To enable a hydrogen-based energy economy, water electrolyzers will play an essential role since these devices can produce pressurized H₂ with relatively high efficiency.² Although electrolyzer technology is already available in the market, higher efficiency, lower degradation, and lower capital cost are needed to meet the Department of Energy's targets for 2025 proton-exchange membrane (PEM) electrolyzers..³ With the anode being one of the largest sources of cell efficiency loss, significant research and development has been directed towards the development of more active, more stable, and lower cost electrocatalysts. Both for acidic and for alkaline applications, material composition and microstructure must be optimized to enhance the rate of the Oxygen Evolution Reaction (OER), thus minimizing the efficiency loss and the amount of noble metal catalysts.⁴⁻⁹ Currently, Irbased catalysts are considered to provide the best balance of activity and stability for acidic PEM water electrolyzers anode catalysts; however, the very high cost and scarcity of Ir (average mass fraction of 0.001 ppm in crustal rock) motivate reducing the amount of Ir required through approaches that increase catalyst activity and lower the catalyst loading. 10-12

Determining the parameters that govern the OER catalytic activity and factors that alter the electrocatalyst durability are primary aspects in the development of new OER electrocatalysts. Given the significant advances in computational chemistry, using a combination of theory and simulations with experimental tools can accelerate the discovery of

materials and processes needed to improve the efficiency of state-of-the-art electrolyzers. One of the main objectives in water splitting research aims to identifying the optimum electrocatalysts capable of accelerating all the stages of the OER. However, composition, material preparation and processing, and morphology all affect electrochemical activity, current selectivity, and stability of oxygen evolution anodes, thus, the development of advanced catalysts can be achieved only if all these factors are fully identified and controlled.¹³⁻¹⁶

Theoretical methods have been broadly applied to determine the factors governing the reactivity of OER electrocatalysts. The overall water-splitting reaction can simply be described by the following reaction:

$$H_2O \to H_2 + \frac{1}{2}O_2$$
 (I)

Gaseous hydrogen and oxygen products evolve from the surface at the cathodic and anodic electrodes, respectively. In acidic media, the anodic reaction is far more sluggish than the cathodic one.¹⁷ One pathway to describe the OER is the *associative* mechanism given by the following reactions,¹⁸ where * denotes a surface site:

$$H_2O \to HO^* + H^+ + e^-$$
 (II)

$$HO^* \to O^* + H^+ + e^-$$
 (III)

$$0^* + H_2 0 \rightarrow H00^* + H^+ + e^-$$
 (IV)

$$H00^* \to O_2 + H^+ + e^-$$
 (V)

Within the associative mechanism, the O-O bond is formed through the association of a water molecule with an O*, as described by reactions IV and V. Although this reaction path is commonly used for modeling the thermochemistry of the electrochemical reactions, other reaction pathways are also possible. For instance, variations of the third step (reaction IV) of this mechanism could result in multiple pathways on how the O-O bond is formed. Rather than proceeding with reactions IV and V, a second possibility is that the O-O bond could be formed

by the association of two O* species, which is described by the following mechanism, known as the direct oxygen recombination pathway:¹⁹

$$0^* + 0^* \to 0_2 \tag{VI}$$

A third option, referred to here as the O and OH recombination mechanism, is that O* combines with a HO* intermediate as depicted in the following reaction:

$$0^* + H0^* \rightarrow H00^* \tag{VII}$$

which is then followed by the subsequent oxidation of HOO* as shown in reaction V.

Recent work has reviewed the OER mechanisms on metal oxides. 12, 20-22 Mechanisms derived from density functional theory (DFT) pioneered by Norskov and coworkers²³ are discussed in the context of the adsorbate evolution mechanism (AEM), which is formulated in the context of a single active site. A modification of such mechanism proposed by Shao-Horn proposes the possibility of two active sites: 6-coordinated and 5-coordinated.²⁴ While the basic chemical and electrochemical reactions proposed in both approaches are the same, the consideration of two sites changes the rate determining step from the OOH formation to the deprotonation of an -OH group stabilizing a -OO group. Deprotonation of this -OH leads to O₂ evolution. Other researchers postulated the participation of the lattice oxygen for the final step of oxygen evolution where an adsorbed oxygen combines with a lattice oxygen atom.²⁵ However, this lattice oxygen mechanism (LOM) may be present only when the catalyst exposes certain facets.²⁶ The advantages of the AEM approach is that it allows relatively easy catalyst screening, based on the characterization of reaction descriptors emerging from a universal scaling relation between the adsorption energies of HOO* vs HO*. 23 Other important concepts arise from cooperative interactions on the surface due to environmental effects such as cooperative hydrogen bonding²⁷ or to surface modifications via dopants or synthesis treatments. 28 29, 30

The electrochemical activity of the electrocatalysts depends to a great extent on the degree of the interaction of the surfaces with the intermediate molecules. Therefore, the oxygen evolution catalysis is restricted by the interdependence of adsorption energies of the reaction intermediates and the surface reactivity.²³ However, changes can occur when a pure surface is doped with another metal either by the exchange of the metal or ligands, i.e., active site modification.^{4, 31} The exchange of metals (i.e., doping) can affect the adsorption of the intermediates directly onto the dopant metal or the neighboring sites, thus affecting not only the reaction rate but possibly the reaction mechanism as well. Moreover, the analysis of the activation barrier for non-electrochemical steps that require the removal and surface diffusion of intermediates is of crucial importance to elucidate the changes caused by selective doping of electrocatalytic surfaces such as IrO₂. For IrO₂ surfaces, significant understanding of the OER mechanisms was obtained from the computational analyses by Ping, Goddard, and collaborators,³² who introduced an innovative approach for the potential-dependence of the reactions, computed reaction energies and activation barriers by DFT at constant potential, and reaction rates based on microkinetic models.

Within our groups' prior study of hydrous nickel-iridium oxide,³³ we showed via experiments and theory that nickel interaction within IrO₂ results in lowering the activation energy and increasing the OER mass and specific activity. However, our prior study considered the direct oxygen recombination and did not consider alternative mechanistic pathways. One of our groups experimentally determined that hydrous cobalt-iridium oxide³⁴ two dimensional (2D) nanoframes exhibit higher activity compared to IrO₂; however, calculations of the effects of Co on the structure and OER mechanism were not explored.

In this work, we combine Density Functional Theory (DFT) and *ab initio* Molecular Dynamics (AIMD) simulations with experimental findings to provide a comprehensive and comparative evaluation of the OER on doped IrO₂ surfaces. The reaction energies and

activation barriers for intermediate steps of the OER are systematically analyzed with different reaction mechanisms on Ni and Co-doped IrO₂ surfaces. The fundamental understanding of the behavior of multiple oxygen evolution mechanisms on these materials provides insight into the effect of doping and assists in design of doping elements or agents to develop new materials for enhanced OER performance in electrolysis processes. Aligned with some of the previous approaches for the OER theoretical analysis,³² this work emphasizes the importance of evaluating the activation barriers for each step of the reaction. Analyzing thermodynamics and kinetics facilitates a comparative analysis with the experimental observations.

2. Methods

2.1. Model and Computational Details

All calculations were performed using the Vienna ab Initio Simulation Package (VASP)³⁵⁻³⁷ employing the projector-augmented wave (PAW) pseudopotentials^{38, 39} to describe electron-ion interactions. The revised Perdew-Burke-Ernzerhof (RPBE) generalized gradient approximation functional was used since it has been found to improve the energies of adsorption transition-metal surfaces.⁴⁰ Spin polarization with cut-off energy for the plane-wave basis expansion of 400 eV were included. The energy convergence criteria for electronic self-consistent iteration and ionic relaxation were set to 10⁻⁴ and 10⁻³ eV, respectively. For structural optimizations and energy calculations, the partial occupancies were represented within the tetrahedron method with Blöchl corrections. The Brillouin zone was sampled using a 11x11x1 Monkhorst-Pack⁴¹ k-point mesh.

Calculations of activation energies were performed using the climbing nudged elastic band (cNEB) method, 42-44 in which a set of intermediate images are optimized along a reaction path defined between the reactants and products. The reactants and products are represented by the initial and final images, respectively, and are optimized before performing the NEB

calculations. In this case, at least 3 intermediate images were used to compute the activation energies (see SI for additional details). Moreover, the charge transfer was investigated using the Bader charge analysis. 45-47 In this method, the electronic charges are approximated by the charge enclosed in a volume defined by zero flux surfaces.

Electrocatalyst Model: To model the pristine and Co- and Ni-doped IrO2 surfaces, the lattice and atomic positions of a bulk IrO₂ unit cell were first fully optimized. The (110) crystallographic plane has been found to be the most stable exposed facet for rutile-type metals such as TiO₂, IrO₂, and RuO₂. ^{18, 48, 49} Thus, a 4-layer (110)-IrO₂ slab was cleaved and a 2x1 supercell was built to represent the surface of the electrocatalyst. A vacuum space of 16 Å was left between the oxide surface and its top neighboring cell images to avoid any interaction. For slab calculations, only the two bottom layers were kept fixed while the positions of the rest of the atoms in the model were allowed to relax. We must note that, in a perfectly cleaved (110) rutile-type oxide, the surface has all metal sites saturated. However, this results on two types of oxygen on the surface: bridge (2-fold coordinated) and undercoordinated (1-fold coordinated). The undercoordinated oxygen species will likely react with water to form molecular oxygen, and once the O₂ is produced a vacancy is formed, leaving the 5-coordinates metal sites exposed, which are active sites for water adsorption.^{31, 33} In this case, the adsorption of water is assumed to start on the unsaturated metal sites and follow the OER until O2 is formed. The resulting surface model is shown in Figure 1a and b, which is formed by four iridium atoms: two penta-coordinated (5-Ir) and two hexa-coordinated (6-Ir) sites. It is worth mentioning that the penta-coordinated sites are also commonly referred as coordinatively unsaturated sites (CUS) in the literature. ^{18, 50} Furthermore, the surface is also comprised of two types of oxygen atoms: four tri-coordinated (O_t) and two bridge or double-coordinated (O_b) oxygen species.

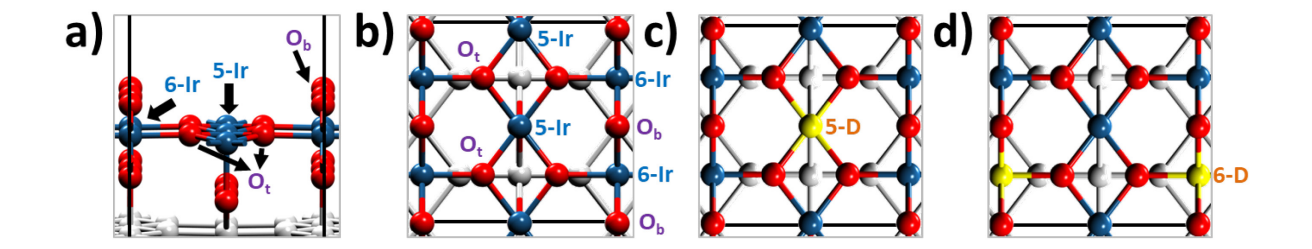


Figure 1. Pristine and doped IrO₂ electrocatalyst model: (a) lateral and (b) top view of the (110) IrO₂ surface. Top view of single-site Co or Ni surface doping at (c) 5-fold (5D-IrO₂) and (d) 6-fold (6-D-IrO₂) coordination sites. Only the top layer is depicted in color for better representation of the surface slab: Ir, blue; Co or Ni, yellow; O, red. *n*-M: *n*-fold coordinated M site (D: Ni or Co dopant; Ir: Ir).

In order to sample different regions of the electrocatalyst, two doped-IrO₂ models were built for each dopant agent depending on the doping site: Co or Ni substituting either 5-Ir or 6-Ir sites on the surface resulting in the 5-D and 6-D sites, respectively, as shown in panels c and d of Figure 1.

Ab initio Molecular Dynamics (AIMD) simulations: to explore the dynamic interaction between water molecules and modeled catalyst surface, AIMD simulations were performed within an NVT ensemble at 300 K during 20000 fs. The hydrogen mass was replaced with the mass of tritium to set a time step of 1 fs. A Nose thermostat with a Nose-mass parameter of 0.5 was used to control temperature oscillations during the simulations. In this case, the Brillouin zone sampling was reduced to a $4\times4\times1$ Monkhorst-Pack⁴¹ k-point grid and a Gaussian smearing with a width of 0.05 eV was employed. The liquid phase was modeled by pure water where the molecules were added to the free volume of the previously optimized IrO₂ slab using the Amorphous Cell packing module as implemented in the BIOVIA Materials Studio software package.⁵¹ This method consists of adding molecules to the free volume in the simulation cell until the target density (ρ_{water} =1 g cm⁻³) is achieved and performing a sequence of classical molecular mechanics-based structural relaxations. The two bottom layers of the slab model and the top layer of water (four molecules) were kept fixed to restrict the dynamic

evolution to only one interface. The liquid model was built in contact with the pristine IrO₂ surface slab and the exact model was replicated for the doped IrO₂ surfaces to allow for a direct comparison between the different models and avoid significant effects due to different liquid conformations. It is worth mentioning that in the real system the electrolyte is not pure water. However, this model still provides a good description since, in this case, we aim to understand the reactivity of water on the catalyst.

Reaction Mechanisms – activation and reaction energies: In the following analysis and discussion of our work we use a different nomenclature for numbering and describing equations than that used in the Introduction (equations I to VII). This is because our study uses elemental steps (e.g. splitting/adsorption of proton and desorption, and electron transfer) instead of overall steps for the various OER stages. Three different reaction pathways are considered in this study. However, they share the same first steps: water adsorption and, subsequent, double oxidation steps to form O* and 2(H⁺+e⁻), as depicted in Eq. 1 and Eq. 2, Figure 2. The differentiating factor between the three mechanisms lies in how the O-O bond is formed. The first mechanism is called direct oxygen recombination, which consists of two water molecules undergoing a two-step oxidation pathway to form two adsorbed O* species, which, then, combine to form O₂ as shown in Eq. 3a, Figure 2. A second pathway evaluated in this study is the recombination of O and OH. In this mechanism, O* combines with a partially oxidized water molecule (*OH) to form a hydroperoxyl group *OOH, Eq. 3b. The *OOH is then oxidized to form O₂ and (H⁺+ e⁻), Eq. 3b.1. Finally, the associative mechanism consists of a water molecule from the liquid phase reacting with an O* group to form an *OOH group, Eq. 3c. This hydroperoxyl group follows the same mechanism as Eq. 3b.1 to form O₂ and (H⁺+ e-).

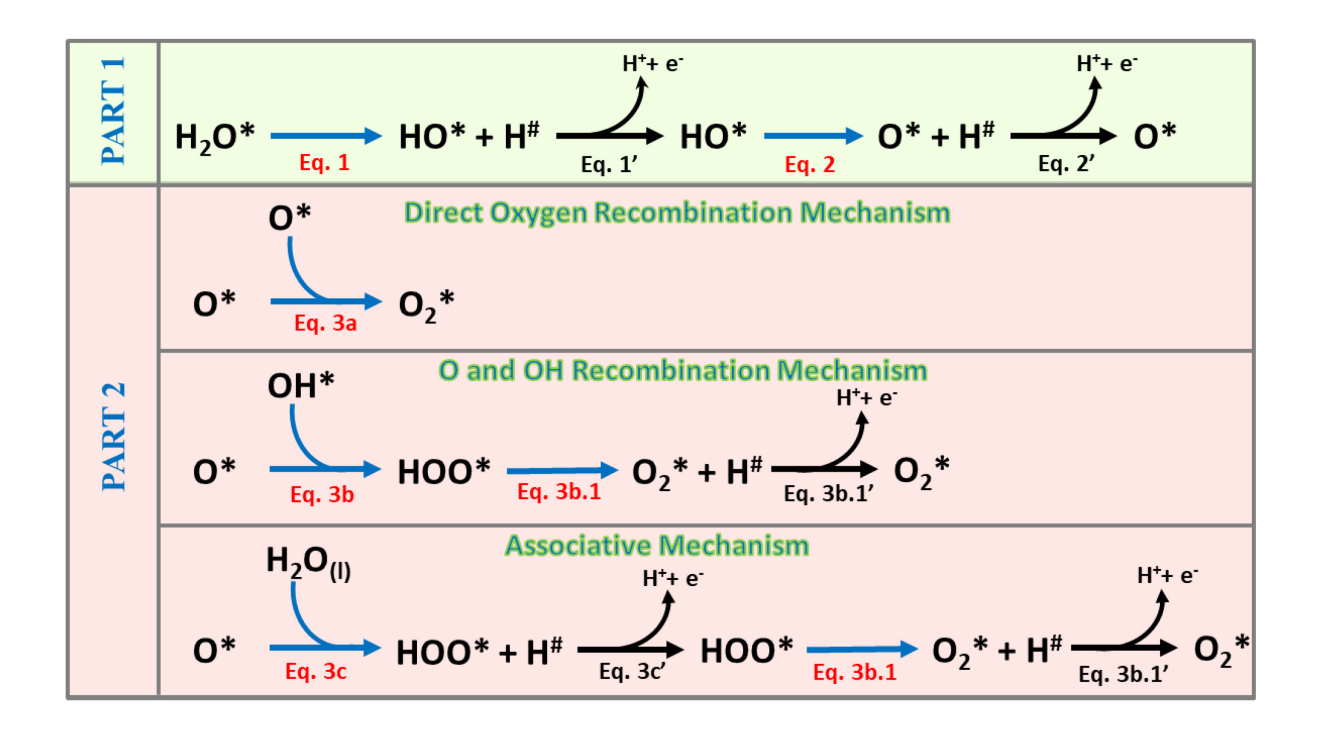


Figure 2. Detailed reaction paths of the oxygen evolution reaction considered in this study. * and * represent an active metal (Ir, Ni, or Co) and O adsorption sites, respectively. Reactions in Part I are common for all three reaction mechanisms. Part 2 represents the three different reaction pathways under investigation depending on how the O-O bond is formed.

Here we consider both a thermodynamic approach and, subsequent estimation of kinetic barriers in order to provide a more comprehensive understanding of how Ni and Co-doping of IrO₂ surfaces affect the OER pathways. Overall, the reaction mechanisms described in Figure 2 include surface reactions followed by electron transfer and proton formation as well as oxygen desorption (not depicted in Figure 2). However, although the energies involved in non-surface reaction steps may influence the overall reaction pathways, we center our attention on those reactions involving surface active sites which are mainly influenced by the electrocatalyst. The surface reactions are highlighted in red in Figure 2: Eq. 1, 2, 3a, 3b, 3b.1, and 3c. Although Eq. 1, 2, 3c, and 3b.1 do not constitute complete electrochemical steps since the proton remains on the surface, in this work, we use such terminology to make it easier for the readers to associate a given step with the actual step in the OER. An example of this is the

use of the terminology "oxidation step" when referring to Eq. 1 and 2. Future work should include the interaction of species being desorbed with the medium, i.e., electrolyte species.

2.2. Experimental Methods

Hydrous nickel-iridium oxide 2D nanoframes and hydrous cobalt-iridium oxide 2D nanoframes were synthesized according to procedures reported in our prior publications^{33, 34} and both treated under the same temperature/reducing atmosphere conditions (300 °C under H₂/Argon). The materials underwent a subsequent chemical leaching step, as described in our prior work, to remove unstable metals. Scanning electron microscopy (SEM) and energy dispersive Xray spectroscopy (EDS) elemental mapping, were obtained with a Helios NanoLab 400 DualBeam Field Emission Scanning Electron Microscope. The samples were prepared by dispersing the catalyst in isopropanol and coating the sample on an aluminum holder.

The electrochemical conditions were reported in more detail previously.^{33, 34} In short, the analysis was carried out at constant temperature (298 K), using a three-electrode cell configuration and a thin-film rotating disk electrode technique (TF-RDE). A gold disk electrode (0.196 cm²) with a thin film of the prepared catalyst was used as the working electrode, a Pt mesh, and a freshly prepared reversible hydrogen electrode (RHE) were used as counter and reference electrodes, respectively. Optimized loadings of 9.1, 15.3 and 11.6 μ g cm_{geo}-² for NiIr, CoIr and IrO₂ respectively, were used for evaluation. The electrochemical characterization of the catalysts was carried out in 0.1M HClO₄ electrolyte prepared with 70% HClO₄ (Veritas Doubly Distilled, GFS Chemicals) (0.000001% Cl) and ultrapure water (\geq 18 M Ω -cm). Prior to the analysis in the OER potential range, the catalysts were electrochemically conditioned by cycling between 0.05 to 1.5 V_{RHE} for 60 cycles at a scan rate of 100 mV s⁻¹ in argon-saturated 0.1 M HClO₄, which is designated as the electrochemical oxidation (EO) step.

The electrochemical surface area of IrO₂ (ECSA_{IrO2}) was then determined by measuring the pseudocapacitive charge between 0.3~V and 1.25~V obtained using a scan rate of $50~mV~s^{-1}$ and by subtracting the contribution of the Au disk current collector. The electrochemical surface area was calculated based on the background subtracted pseudocapacitive charge and the coulombic conversion factor of 596 mC cm_{IrO2}⁻¹.52 The oxygen evolution reaction activity, was determined by performing steady-state (iR-corrected) chronoamperometric measurements by stepping the potential at steps of 0.01 V from 1.3 to 1.6 V_{RHE} while holding for 5 seconds at each potential and rotating the working electrode at 2500 rpm. The internal resistance (iR) values (23–27 Ω) was determined prior to every evaluation using the current interruption method at 1.6 V_{RHE}. The data obtained from chronoamperometric measurements was used for the Tafel plots and for determining the OER mass activity and specific activity. The activation energy was calculated using the exchange current density estimated by the extrapolation of the Tafel slopes, where current was normalized by the electrochemical surface area, to 1.23 V_{RHE}. Following the measurements of the OER activity, an accelerated durability test was carried out by maintaining the electrode at a constant potential of 1.6 V_{RHE} for 13.5 hours under a rotation rate of 2500 rpm. The evaluation of the electrochemical activity after durability test (ADT), was carried out using the same procedure as used for the EO step, as described above.

3. Results and Discussion

3.1. Interfacial Evolution between Liquid Water and IrO₂ and doped-IrO₂ Surfaces from AIMD Simulations

Figure 3 describes the evolution process of a pristine IrO₂ surface when placed in contact with liquid water at room temperature. In this case, no external potential is applied to the simulation box, so that the results are comparable with our predictions of reaction and activation energies. During the first 500 fs of the AIMD simulation, two water molecules are

attracted to the 5-fold coordinated Ir sites and become adsorbed as shown in the first three panels in Figure 3. Remarkably, at around 700 fs, one of the adsorbed water molecules breaks to form OH and H. While OH remains adsorbed on the Ir site, the H species bonds with a bridge oxygen from the surface (O_b). At 900 fs, a water molecule from the liquid phase positions between the other adsorbed molecule and acts as a proton acceptor and donor to split the second water molecule to OH and H at around 3400 fs. Similar to the previous case, OH remains adsorbed on the 5-fold coordinated Ir site and H is bonded to the second bridge oxygen. In this scenario, however, the H was coming from a water molecule in the solution. Nevertheless, the final products are the same. OH and H species remained adsorbed to 5Ir and Ob sites, respectively, and no further reactions were evidenced from this point until the end of the AIMD simulation (20 ps). The dissociative behavior of water on the IrO₂ (110) surface agrees with the early prediction of Scheffler and collaborators⁵³ obtained via static DFT and ab initio thermodynamics predictions of the evolution of the (110) RuO2 surface under humid environments. Moreover, DFT and AIMD analyses reported recently by Sudope et al. ²⁷ reveal the effect of cooperative H-bonding and adsorption interactions with distorted octahedral rutile oxide surfaces, showing clear differences between the water behavior over TiO₂ (molecular adsorption) vs. RuO₂ and IrO₂ surfaces (dissociative adsorption). Our DFT and AIMD results are also in good agreement with these observations regarding IrO₂.²⁷

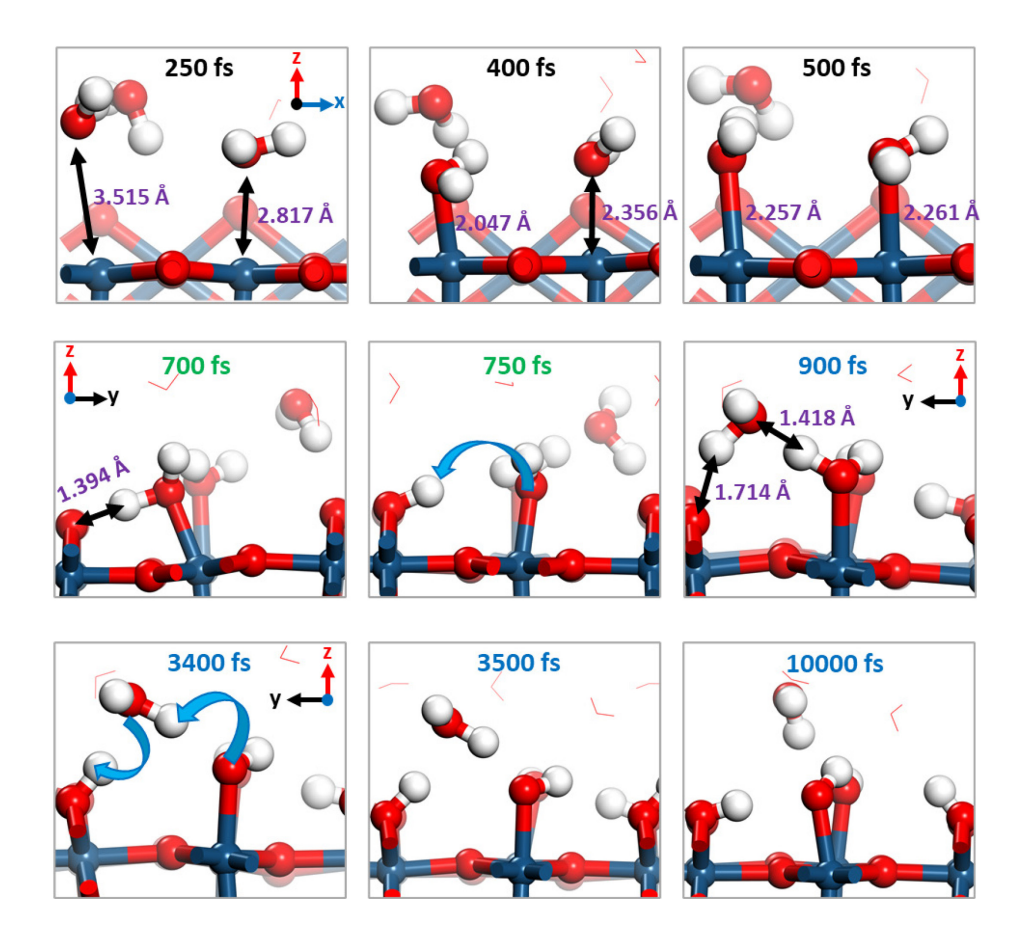


Figure 3. Dynamic evolution of water molecules interacting with a pristine IrO₂ slab along the AIMD simulation. Blue arrows represent the movement of hydrogen species. Atoms at the interface level are depicted using the ball-and-stick model and water molecules not involved are shown as thin sticks for better representation of the interface. Color code: Ir, blue; Co or Ni, yellow; O, red; H, white. Different colors are used for the timestamps to distinguish the orientation of the cell used to take each frame.

Similarly, the above-mentioned behavior is also observed when the IrO₂ surfaces are doped; water molecules are adsorbed on the 5-fold coordinated sites (Ir, Co, or Ni). The MeO₁ bond distances are tracked along the AIMD simulation, and the results are reported in Figure S1. In every case, water molecules become adsorbed within the first 1000 fs of simulation. However, a key difference between the multiple surfaces studied is that no water splitting was observed during the simulated time when water adsorbed on a doped site (Co or Ni). The simulated time that took each water molecule to split into OH and O (Eq. 1, Figure 2) is presented in Figure 4. It is noteworthy that only one molecule is split on 5Co-IrO₂ and 5Ni-IrO₂ surfaces. This is because there are two 5-fold coordinated sites and one of them is doped,

where no splitting occurred during the time of the AIMD simulation. On the other hand, both adsorbed water molecules react to form OH and H relatively faster on 6Ni-IrO₂ and 6Co-IrO₂ surfaces than pristine IrO₂. It is important to note that although these observations are qualitative reflection of the surface reactivity, we can still use them in the analysis of the calculated reaction and activation energies.

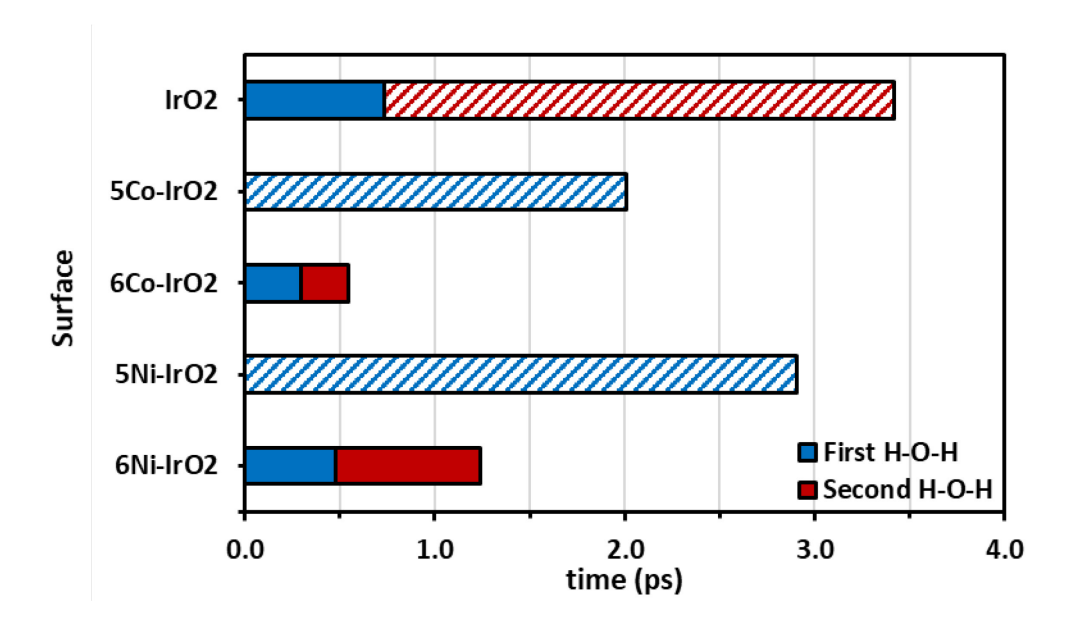


Figure 4. Time to first water splitting reaction ($H_2O \rightarrow OH$ and H) obtained from the AIMD simulations. Blue and red colors indicate two different water molecules, which are adsorbed on 5-fold coordinated sites. Solid bars represent the direct H transfer from the adsorbed water molecule to the bridge oxygen, whereas bars with diagonal stripes depict those cases where a water molecule from the solution (non-adsorbed) servers as a proton acceptor and donor as shown in the panel at 3000 fs in Figure 3.

Table 1. Reaction (ΔE_i) and activation (ΔE^{act}_i) energies for the first and second water splitting reactions (water oxidation: O-H bond cleavage): Eq. 1 and Eq. 2 in Figure 2. Results from pristine and Co-doped IrO₂ and Ni-doped IrO₂ surfaces were taken from our previous reports: Gonzalez-Huerta *et al.*³¹ and Godínez-Salomón *et al.*,³³ respectively, and are summarized here for comparison purposes. Site (5-Ir, 5-Co, or 5-Ni) indicates where the water molecule was initially adsorbed.

Surface: Site	Energies in eV					
Surface: Site	$\Delta \mathbf{E^{act}}_1$	$\Delta \mathbf{E}_1$	$\Delta \mathrm{E}^{\mathrm{act}}{}_{2}$	$\Delta \mathrm{E}_2$		
p-IrO ₂ : 5-Ir	-	-0.47	0.56	0.18		
5Co-IrO ₂ : 5-Ir	-	-0.37	0.48	0.19		
5Co-IrO ₂ : 5-Co	0.20	0.00	0.47	0.11		
6Co-IrO ₂ : 5-Ir	-	-0.72	0.45	-0.12		
5Ni-IrO ₂ : 5-Ir	-	-0.35	0.81	0.15		
5Ni-IrO ₂ : 5-Ni	0.29	0.24	0.74	0.68		
6Ni-IrO ₂ : 5-Ir	1	-0.82	0.38	-0.23		

Table 1 summarizes the energies of reaction and activation for the first and second water splitting reactions (O-H bond breakages), which had been reported in our previous publications.^{31, 33} The energies of reactions were computed using the following equations:

$$\Delta E_1 = E_{H^{\#} + HO^*/cat.} - E_{H_2O^*/cat.}$$
 3.1.1

$$\Delta E_2 = E_{H^\# + O^*/cat.} - E_{HO^*/cat.}$$
 3.1.2

where $E_{i/cat}$ is the energy of the catalyst surface with the adsorbed species i, and * and # are the adsorption sites; *: 5-fold coordinated metal site, #: bridge oxygen site. The sites specified in Table 1 (5-Ir, 5-Co, or 5-Ni) represent the metal site where the water molecule was initially adsorbed. As shown in Table 1, the energy of first oxidation step, ΔE_1 , is exothermic ($\Delta E < 0$) with no activation barrier when the water molecule is adsorbed on a 5-Ir site. However, energetic barriers, ΔE^{act}_{1} , rise for this step when the adsorption occurs on a doped site (5-Co or 5-Ni). This is in good agreement with the results found from AIMD simulations where no water splitting is observed when adsorption initially occurs on a doped site. However, when the dopant is located in a 6-fold coordinated site (6-D), the reaction becomes even more favorable, which may correlate with the relatively faster oxidation process found in our AIMD simulations for both adsorbed water molecules in systems with barrierless first oxidation step. As discussed in our previous works, ^{31, 33} the presence of the dopant on 6-D sites alters the electronic charge around bridging oxygen atoms, which act as proton acceptors in this reaction step, resulting in a higher driving force for the first O-H bond cleavage. In contrast, the energy of second O-H bond cleavage, ΔE_2 , is endothermic ($\Delta E > 0$) on undoped IrO₂ surfaces, and although this process becomes slightly exothermic with the presence of dopant in the 6-D sites, the activation barriers, ΔE^{act}_{2} , are significantly higher than those in the first reaction step, ΔE^{act}_{1} . This could explain why the second oxidation step is not seen during the timescale of the AIMD simulation

without an applied external potential. The resulting optimized structures from the reaction and activation energies are reported in Figure 5a and b. Bond distances associated with the reaction mechanism are also included in each panel for reference.

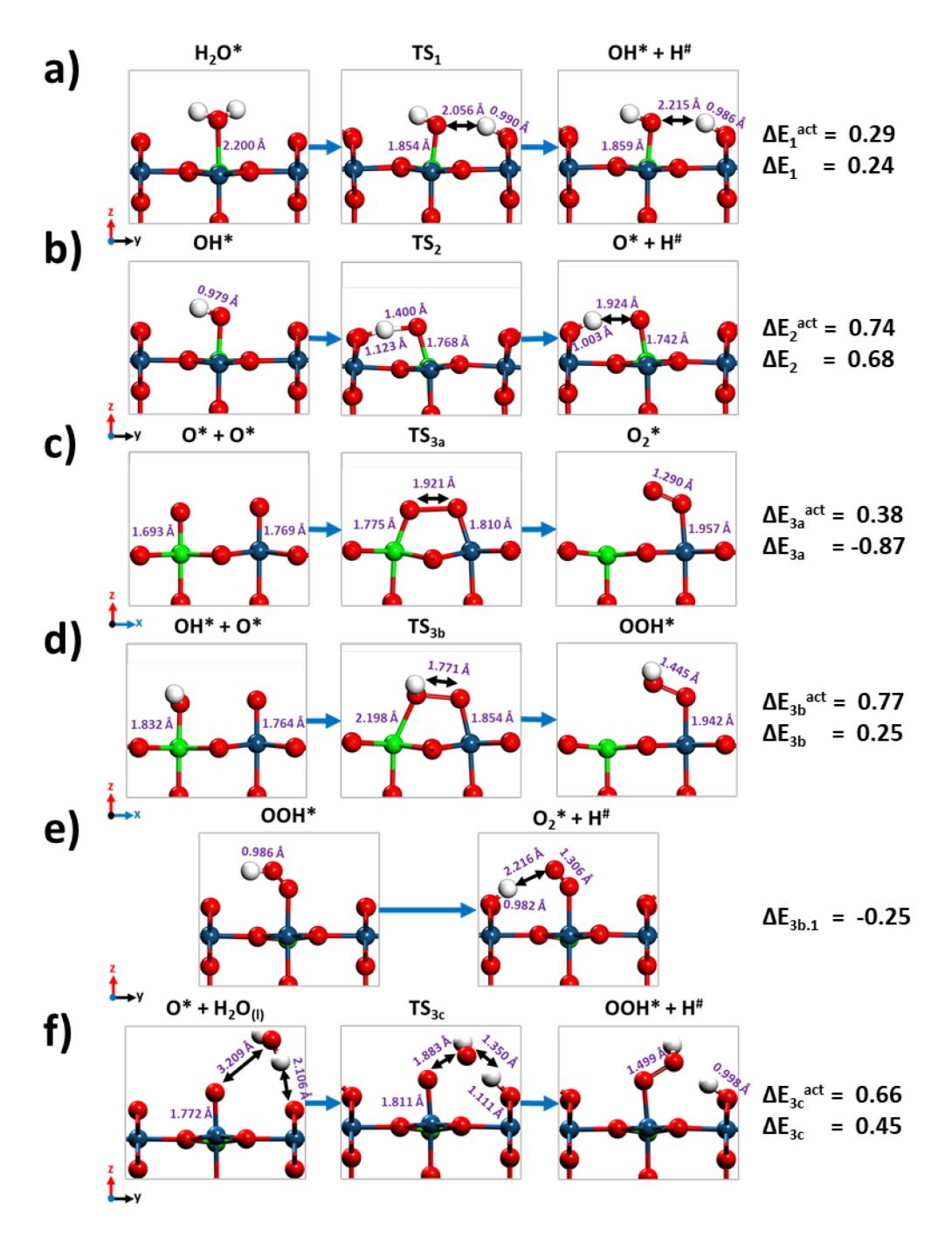


Figure 5. Resulting optimized initial and final, and transition state structures (TS_i) for all the reaction mechanisms considered in this study on a sample surface (5Ni-IrO₂). Panels represent equations described in Figure 2: a) Eq. 1; b) Eq. 2; c) Eq. 3a; d) Eq. 3b; e) Eq. 3b.1; and f) Eq. 3c. Color code: Ir, blue; Ni, green; O, red; H, white. Structures obtained when other surfaces are used are similar and, therefore, not shown here. These structures are available to readers upon request. Note about panel e) the OOH group was slightly rotated and re-optimized to ease the calculation of transition state for the

oxidation of OOH. Once optimized, the change in energy was found to be, on average, less than 0.04 eV, and no changes to the trends were found. Reaction (ΔE_i) and activation (ΔE_i^{act}) energies in eV for the sample surface are reported on the right side of the figure. These energies are reported here for reference and will be discussed in the following sections in detail.

3.2. Reaction Mechanisms: O-O bond formation

The water oxidation steps described in the previous section are shared for all the three reaction pathways considered in this study. In this section, we focus our attention on the steps leading to the formation of the O-O bond and the formation of O2. In any of the reaction pathways considered at least one water molecule must undergo a double O-H bond cleavage, resulting in the formation of an adsorbed O* species as shown in Figure 2. This O* species can then react with a water molecule or one of the intermediates of water splitting (O or OH) to subsequently form the O-O bond. It is assumed that for the recombination mechanisms (Eq. 3a and Eq. 3b), the intermediates are still adsorbed on the same sites where the water molecules were initially adsorbed. Therefore, a difference in the adsorption strength of the intermediate species could yield lowered energetic barriers when combining O with either OH or O (nonelectrochemical steps). Thus, we have evaluated the adsorption strength of OH and O on the 5fold coordinate doped site of an IrO₂ surface. For this, the pristine IrO₂ surface model was taken and one of the 5-Ir was substituted with multiple transition metals (Ag, Au, Cu, Co, Ni, Os, Pd, Pt, Rh, and Ru). The calculated adsorption energies of OH and O, which are given by the $E_{ads_i} = E_{i/cat.} - (E_i + E_{cat.})$ expression, are reported in Figure S2. The adsorption of O and OH on a 5-Ir site is -4.23 and -3.06 eV, respectively. However, the adsorptions of these species on a doped Ni or Co site have intermediate strength, which could result in a lowered energetic requirement for desorbing and moving OH or O to a different site to form the O-O bond. Besides, the adsorption energy is strong enough that the adsorption can still occur. The adsorption energy of O and OH on a 5-Co (5-Ni) site is -3.09 and -1.91 eV (-2.21 and -1.64

eV), respectively. Thus, the trend in adsorption strength for metallic sites would be 5-Ir > 5- Co > 5-Ni on the IrO₂ electrocatalyst.

To study the water splitting steps given by the reactions in Eq. 3a, 3b, and 3c (Figure 2), we start by considering the intermediate adsorbed species that would give place to one of the recombination mechanisms (O and O or O and OH) or the associative mechanisms (O plus H₂O(h)). An example of the structural configuration of these adsorbed species is shown in Figure 5c, d, and f for direct oxygen recombination (eq. 3a), O and OH recombination (eq. 3b), and associative mechanisms (eq. 3c), respectively. In every case, the adsorption element is an O species. The electronic charge transferred from the electrocatalyst to the species involved in the reactions is reported in Table 2. The adsorption of O on the dopant site (5-D) results in less charge transfer and a weakened adsorption strength. In the case of the adsorption of OH, no significant impact on the transferred charge is observed. Finally, the H₂O molecule in the associative mechanism (3c) slightly losses some charge most likely due to the interaction of H with bridge oxygen atoms from the surface; however, the change is minimal as expected due to its non-adsorbed nature.

Table 2. Electronic charge (in |e|) transferred from electrocatalyst to adsorbed species. Underlined and italicized values indicate adsorption on the doped site; * represents the site where the species containing the O-O bond remains adsorbed after the reaction.

Surface: Site	Mechanism 3a		Mechai	nism 3b	Mechanism 3c	
	O*	0	O*	OH	O*	H ₂ O _(l)
p-IrO ₂ : 5-Ir	-0.48	-0.47	-0.49	-0.30	-0.49	0.03
5Co-IrO ₂ : 5-Ir	-0.47	<u>-0.44</u>	-0.53	<u>-0.26</u>	-0.49	0.05
5Co-IrO ₂ : 5-Co	<u>-0.44</u>	-0.47	<u>-0.48</u>	-0.29	<u>-0.38</u>	0.01
6Co-IrO2: 5-Ir	-0.48	-0.48	-0.51	-0.29	-0.46	0.04
5Ni-IrO2: 5-Ir	-0.41	<u>-0.37</u>	-0.42	<u>-0.32</u>	-0.48	0.03
5Ni-IrO2: 5-Ni	<u>-0.37</u>	-0.41	<u>-0.40</u>	-0.30	<u>-0.35</u>	0.07
6Ni-IrO2: 5-Ir	-0.47	-0.43	-0.44	-0.29	-0.52	0.02

Direct oxygen recombination mechanism: The reaction and activation energies for the reaction described by Eq. 3a are presented in Figure 6. The energy of reaction was computed using the following equation:

$$\Delta E_{3a} = E_{O_2^*/cat.} - E_{O^*+O^*/cat.}$$
 3.2.1

The results for pristine IrO2 and Ni-doped IrO2 were obtained from our previous work³³ and are presented here for discussion. The reaction energy to form O₂ from two adjoined adsorbed O* species on a pristine IrO₂ surface was found to be 0.82 eV with no transition state.³³ Doping IrO₂ on 6-fold coordinated sites (6Co- or 6Ni-IrO₂) was found to make this reaction step slightly less favorable than on pristine IrO₂ surfaces: 1.03 eV on 6Co-IrO₂ (Figure 6a) and 0.91 eV on 6Ni-IrO₂ (Figure 6b). However, the presence of the doping agent on a 5-fold coordinated site was found to diminish the energy of reaction significantly; the effect is more pronounced when the formed O_2 is adsorbed on the 5-Ir site: ΔE_{3a} was predicted to be 0.01 eV and -0.87 eV on 5Co-IrO₂ and 5Ni-IrO₂ surface, respectively. As previously discussed, the adsorption strength of atomic oxygen on the 5C sites directly correlates with the energy of reaction for this step. Adsorption of O on a 5-Ir site was found to be -4.23 eV, whereas this strength (adsorption energy) was diminished by 27% and 48% when the adsorption occurred on 5-Co and 5-Ni sites, respectively. Therefore, the lower the strength of adsorption of one of the sites where O has adsorbed the more favorable energy of reaction appears to be. Overall, the 5Ni-IrO₂ surface was found to perform better for the oxygen recombination reaction step than the 5Co-IrO₂. The activation energy for 5Co-IrO₂ (0.85 eV) was predicted to be comparable with the energy of reaction on pristine structures (0.82 eV). However, this barrier is remarkably reduced (~0.38 eV) on 5Ni-doped electrocatalysts. The resulting structures for this reaction step on 5Ni-IrO₂ (O₂ adsorbed on 5-Ir site) are reported in Figure 5c.

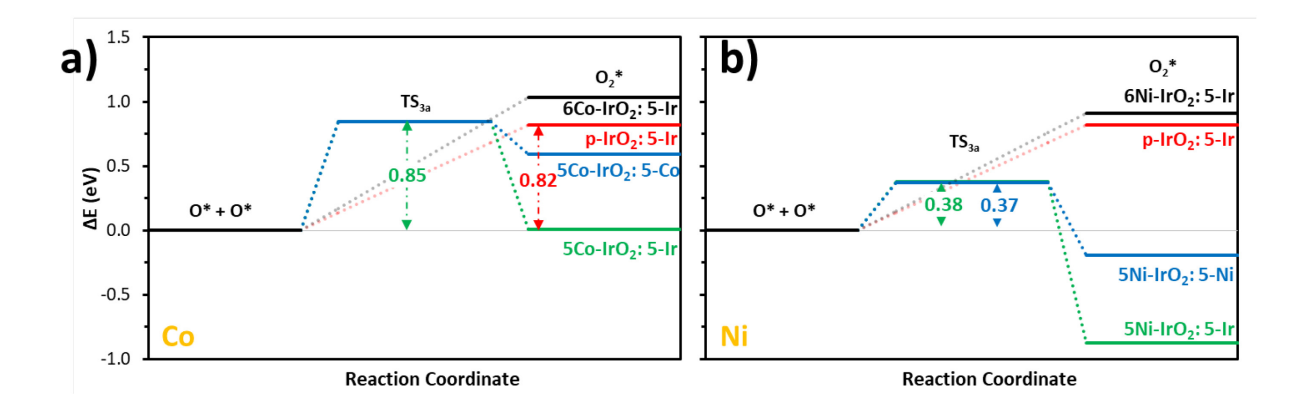


Figure 6. Relative reaction and activation energies for the oxygen recombination step (Eq. 3a in Figure 2) of the OER on pristine (p),³³ (a) Co-doped and (b) Ni-doped³³ IrO₂ electrocatalysts. In the case of 5D-IrO₂ systems, two curves are shown depending on the adsorption site (5-Ni or 5-Ir) of the resulting molecule. TS_{3a} indicates the transition state for the oxygen recombination step. The legend defines the surface and the final adsorption site (*surface*: *site*). Raw values for this step are tabulated in Table S1.

An important consideration to account for in the formation of O_2 in the direct oxygen recombination mechanism is the O-O bond distance in O_2 due to potential errors typically seen in gas-phase DFT calculations. For that reason, the O-O bond distances of O_2 * adsorbed species have been evaluated for all the systems, and the data is presented in Table S2. Our findings show that the O-O bond lengths range between 1.26-1.30 Å. These results agree with reported O-O bond lengths for adsorbed O_2 - (1.28 Å)⁵⁴. In addition, the O_2 - bond length is in the range of values calculated for adsorption of O_2 on small Pt clusters⁵⁵. The bond length for molecular oxygen, on the other hand, is ~1.21 Å. These results provide additional support for the validity of the methods used in this work.

O and **OH** recombination mechanism: The energy of reaction for this step is given by the following equation:

$$\Delta E_{3b} = E_{OOH^*/cat.} - E_{O^* + HO^*/cat.}$$
 3.2.2

Despite the OH adsorption being considerably weaker than the O (Table 2), the recombination of O and OH was found to be less favorable than that of oxygen, see Figure 7. Weak interactions of the OH group with oxygen atoms from the surface may be causing the OH motion over the surface to be less energetically favorable leading to higher activation and reaction energies despite its lower adsorption strength on the metallic sites. Figure 7 shows that the ΔE_{3b} is 1.49 eV when the reaction occurs on an undoped surface. However, the reaction energy decreases substantially on 5D-IrO2 surfaces, especially when the formation of the hydroperoxyl group (OOH) occurs on the 5-Ir site. Similar to the case of direct oxygen recombination, the lower the adsorption strength of the OH the more favorable the energy of reaction becomes. Once again, the reaction energy for Eq. 3b is found to be less endothermic when the surface is doped with Co or Ni on a 5C site – 0.51 eV and 0.25 eV, respectively – and the effect is more marked when the OOH is formed on the 5-Ir site leaving the site where OH was initially adsorbed vacant. When doping is performed on a 6C site, the ΔE_{3b} 's are found to be similar to those of the undoped surfaces. However, the activation energy is higher (\sim 7%) on 6Co-IrO₂ than the p-IrO₂ electrocatalyst. In the case of 6Ni-IrO₂, both activation and reaction energies are comparable with those of the pristine surface. The activation energies for the hydroperoxyl formation are considerably diminished for 5D-IrO₂ surfaces: up to 34% and 55% in the case of 5Co- and 5Ni-IrO₂ structures, respectively. Interestingly, although the reaction energy is significantly lower for 5Ni-doped systems when the OOH is formed on the 5-Ir site, the activation energy is slightly lower (0.77 vs 0.68 eV) when the OOH is formed on the 5-Ni site, which stresses the importance of evaluating not only the thermodynamics but also the kinetics of the reactions. The resulting structures for this reaction step on 5Ni-IrO₂ (OOH formed on 5-Ir site) are reported in Figure 5d.

The energy of reactions for the oxidation of the OOH (Eq 3b.1; an example of the optimized structure is shown in Figure 5e) to form molecular oxygen, which is given by the following equation:

$$\Delta E_{3b.1} = E_{O_2^* + H^{\#}/cat.} - E_{OOH^*/cat.}$$
 3.2.3

is reported in Figure 7. This reaction step was found to be exothermic and, in most cases, barrierless for all the studied systems – in a couple of cases (see Table S3), transition states with activation energies of less than 0.02 eV were found (not shown in Figure 7); however, these can be neglected for this study. Similar to the behavior observed for reactions involving proton transfer (Eq. 1 and 2), the doping of 6-fold coordinated sites was found to lead to the most favorable reaction energies – $\Delta E_{3b.1}$ was calculated to be -0.43 and -0.75 eV for Co- and Ni-doped IrO₂, respectively. For 5D-IrO₂ systems, Co-doping was found to yield more favorable reaction energies than Ni-doping.

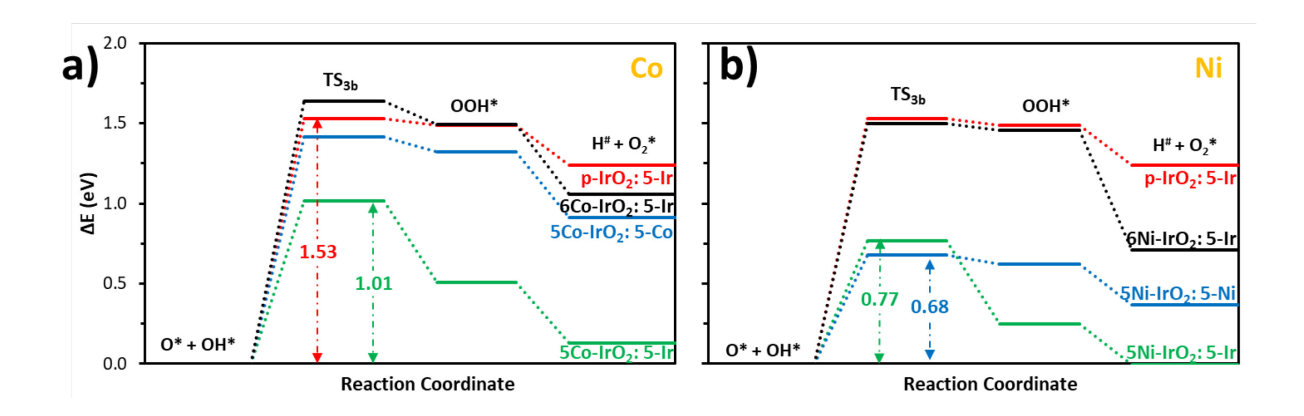


Figure 7. Relative reaction and activation energies for the O and OH recombination (Eq. 3b in Figure 2) and OOH oxidation (Eq. 3b.1) steps of the OER on pristine (p),⁵⁶ (a) Co-doped,⁵⁶ and (b) Ni-doped IrO₂ electrocatalysts. In the case of 5D-IrO₂ systems, two curves are shown depending on the adsorption site (5-Ni or 5-Ir) of the resulting molecule. TS_{3b} indicates the transition state for the O and OH recombination step. The legend defines the surface and the final adsorption site (*surface*: *site*). Raw values for these reaction steps are tabulated in Table S3.

Associative Mechanism: This mechanism assumes that only one water molecule undergoes full oxidation to O due to direct contact with the surface, while the second molecule will react with the formed O to produce the hydroperoxyl group as a reaction intermediate.

This step is described by Eq. 3c and the resulting optimized initial and final, and transition state structures for one of the systems (5Ni-IrO₂: 5-Ir) are reported in Figure 5f. The reaction energies were calculated using the following expression:

$$\Delta E_{3c} = E_{OOH^* + H^{\#}/cat.} - E_{O^*/cat. + H_2O}$$
3.2.4

and the results are presented in Figure 8. When the reaction takes place on an undoped surface, the energy of the reaction is 0.45 eV with an activation energy of 0.66 eV. In the case of 5D-IrO₂ systems with the OOH formation on 5-Ir sites, the energies of activation and reaction for this step are similar to those obtained when the OER occurs on undoped. Conversely, if a 6fold coordinated site is doped with either Ni or Co, the energy of reaction for this reaction step (0.20 eV) is diminished by 56% when compared with the pristine electrocatalytic surface. Similarly, the activation barrier for this step is also lowered by 18% (11%) in the case of Codoped surfaces (Ni-doped). This behavior is in good agreement with our previous findings on steps of the OER involving proton transfer, where 6D-IrO₂ systems have been found to perform better than pristine IrO₂ and, in many cases, better than 5D-IrO₂ surfaces as well.^{31, 33} A remarkable behavior seen with this reaction mechanism is that, if the reaction takes place on the O* adsorbed on the doped site of a 5Ni-IrO2 surface, the reaction becomes exothermic $(\Delta E_{3c}=-0.38 \text{ eV})$ with an activation barrier of 0.51 eV, which is 23% lower than the IrO₂. On the other hand, a different behavior is seen on 5Co-IrO₂ (OOH formed on the 5-Co site). In this case, the reaction energy is similar to that of the undoped anode, and the activation energy is found to be considerably higher (0.92 eV). The oxidation step of OOH is the same as the one given by Eq 3b.1, which was discussed in the previous subsection.

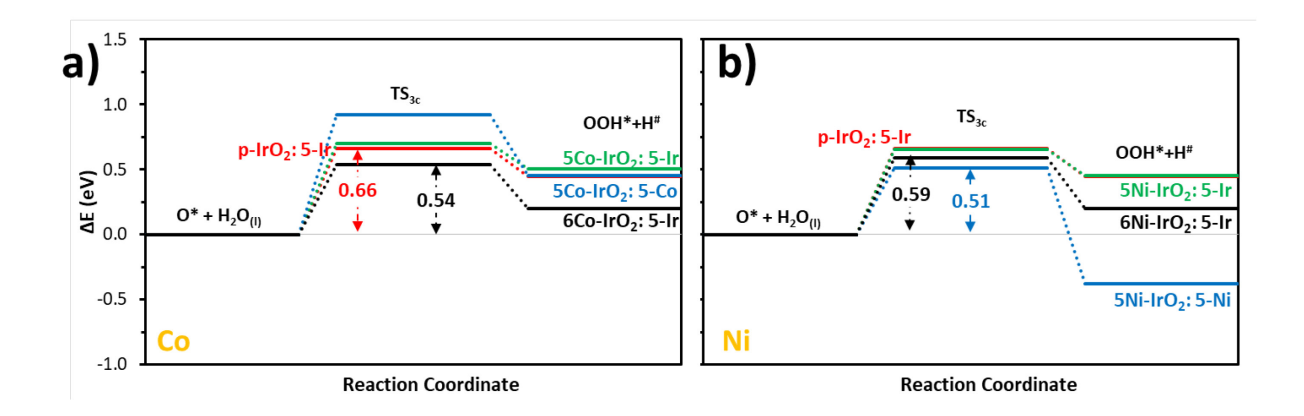


Figure 8. Relative reaction and activation energies for the associative step (Eq. 3c in Figure 2) of the OER on pristine (p), (a) Co-doped, and (b) Ni-doped IrO₂ electrocatalysts. In the case of 5D-IrO₂ systems, two curves are shown depending on the adsorption site (5-Ni or 5-Ir) of the resulting molecule. TS_{3c} indicates the transition state for the associative step. The legend defines the surface and the final adsorption site (*surface*: *site*). Raw values for this step are tabulated in Table S4.

3.3. Double doping of IrO₂ surfaces

In the previous section, the performance of the doped electrocatalytic surfaces was found to be dependent on the site of the surface that is doped. Therefore, the effect of doping the IrO₂ surface on both penta- and hexa-coordinated sites was evaluated to understand such synergistic effects. A similar approach to the one described in the previous section was followed. However, in this case, two Ir sites (5-Ir and 6-Ir) are substituted with the dopant element within the surface layer yielding to 2xD-IrO₂ surfaces, where D is the dopant metal (Co or Ni). Electronic density difference ($\Delta \rho = \rho_{2xD-IrO_2} - \rho_{IrO_2}$) due to the double doping is reported in Figure 9. It can be seen that the effect of doping is qualitatively the same regardless of the metal used for doping; significant electron accumulation (purple) is evidenced at the doped sites and depletion (yellow) between the doped site and the neighboring oxygen atoms. It is noteworthy that the presence of the dopant in the 6-fold coordinated site yields a strong accumulation of electron density around its bonding oxygen atoms including the bridge oxygen atoms, which can serve as proton acceptors during multiple steps of the OER. Overall, the effect of doping on the electron density seems to follow an additive behavior of those of the single doping system as discussed in our previous work.^{31,33} Therefore, similar changes to

the chemical environments of both doped sites are expected to yield a synergistic effect on the catalytic activity of the anode on the OER when compared to the single doped surfaces.

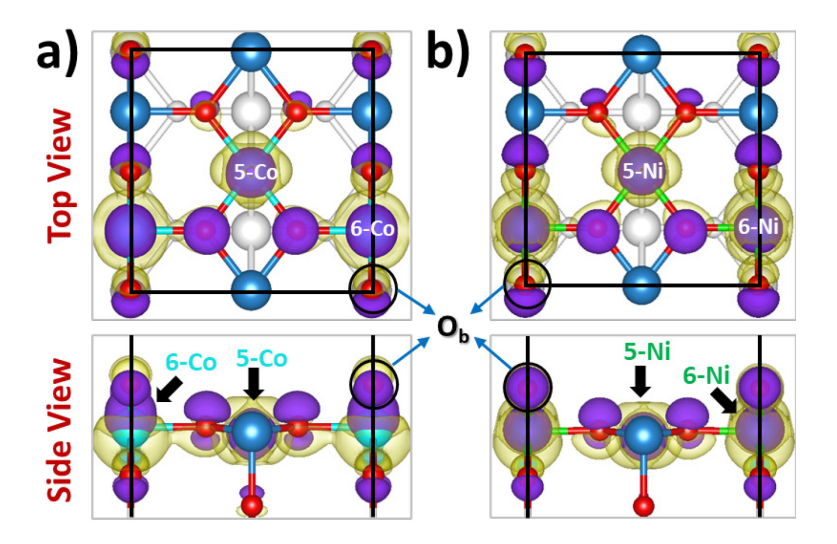


Figure 9. Electronic density accumulation (purple)/depletion (yellow) on the surface plane of (a) 2xCo-IrO₂ and (b) 2xNi-IrO₂ structures. Surface layer color code: O, red; Ir, blue; Co, light blue; Ni, green. Black lines depict the edges of the simulation cell. Subsurface atoms are shown in white.

The reaction and activation energies for the first and second water oxidation steps were calculated and are reported in Table 3. The first oxidation step (Eq. 1) is found to be barrierless when the water is adsorbed on a 5-Ir site and the energy of reaction is significantly more favorable – -0.81 and -0.66 eV for Co- and Ni-doped IrO₂, respectively – than on pristine surfaces (-0.47 eV). It is noteworthy that this step was found to be slightly endothermic and to have an activation barrier (> 0.20 eV) on singled doped 5D-IrO₂ surfaces when the adsorption took place on the 5D site (Table 1). In this case, however, although the reaction energy is less favorable than p-IrO₂, the process is still exothermic and just a small activation barrier is predicted (< 0.10 eV). This difference can be attributed to the presence of a second dopant on the hexa-coordinated sites, which have been found to facilitate the reaction steps of the OER involving proton transfer. On the other hand, the second oxidation step (Eq. 2) is found to be endothermic (0.18 eV) with an activation barrier of 0.56 eV on IrO₂ surfaces. However, when

the surface is double doped with Co, the reaction becomes exothermic (~-0.10 eV) and the activation barrier is lowered to 0.36-0.47 eV, which is also an improvement from the single doped surfaces. Similar behavior is exhibited for surface double doped with Ni when compared with single doping. However, in this case, the activation barriers are comparable with those of the undoped electrode. Interestingly, the energy of reaction considerably differs depending on where the OH is adsorbed; -0.28 eV and 0.31 eV when adsorbed on 5-Ir and 5-Ni sites, respectively.

AIMD simulations (20 ps) of these two double-doped surfaces in contact with liquid water showed similar behavior to the one observed on the single doped IrO₂ systems. The first oxidation of the water is seen when the molecule is adsorbed on the 5-Ir site. This is a good agreement with our predicted activation and reaction energies. In the case of water molecules that are adsorbed on the 5-D site, the driving force is much smaller for the reaction to occur. In addition, there is a small activation barrier that needs to be overcome, which, similar to single doped surfaces, is likely the reason no reaction is observed during the timescale of the simulation. Thus, only one molecule of water reacted in each case, see Figure S3 and Table S5. At 490 fs, a water molecule reacted on the 2xCo-IrO₂ surface, and a water molecule in the solution acts as proton acceptor-donor to assist in the reaction, similar to what is seen in the frame at 3400 fs in Figure 3. Conversely, the water molecule that reacts in the 2xNi-IrO₂ system transfers its proton directly to the bridge oxygen from the surface at 360 fs.

Table 3. Reaction (ΔE_i) and activation (ΔE^{act}_i) energies for the first and second water oxidation steps (Eq.'s 1 and 2 in Figure 2) on doubled doped surfaces. Site (5-Ir, 5-Co, or 5-Ni) indicates where the water molecule was initially adsorbed.

G C G	Energies in eV					
Surface: Site	ΔE ^{act} 1	ΔE_1	ΔE ^{act} 2	ΔE_2		
2xCo-IrO2: 5-Ir	-	-0.81	0.47	-0.09		
2xCo-IrO2: 5-Co	0.06	-0.24	0.36	-0.10		
2xNi-IrO ₂ : 5-Ir	-	-0.66	0.58	-0.28		
2xNi-IrO ₂ : 5-Ni	0.10	-0.14	0.56	0.31		

Reaction and activation energies for Equations 3a-c, which is where the three reaction mechanisms being studied differ from each other, are tabulated in Table 4. No significant changes are seen for non-electrochemical steps such as Eq. 3a and 3b when compared to their equivalent systems in single doping (5D-IrO₂) systems. Thus, although some fluctuations in the absolute values for the predicted energies, these are still comparable with our analysis in the previous section. As such, the presence of Ni or Co on a hexa-coordinated site may not have a notorious impact on the reaction and activation energy of the non-electrochemical steps. On the contrary, the presence of 6-D sites on the IrO₂ surface makes the proton transfer from OOH to form O₂ ($\Delta E_{3b,1}$) considerably more favorable (i.e., more exothermic) than when the reaction takes place on undoped or 5D-doped electrodes. In the case of the associative mechanism (Eq 3c), the presence of the 6Co site results in a lowered energy of reaction when compared to those calculated using 5Co- and p-IrO₂ models. However, the activation energy for this step is still higher than that obtained from the pure IrO₂ (0.66 eV). On the other hand, if the reaction takes place on a 2xNi-IrO₂ and the OOH is formed on a 5-Ir site, the activation energy (0.63 eV) is comparable with that of the undoped system. However, the energy of reaction is reduced by 36% if the OOH is formed on a 5-Ni site, although the activation energy is similar to the one for 5Ni-IrO₂ systems. However, the step becomes more exothermic – e.g., ΔE_{3c} lowers from -0.38 to -0.66 eV.

Table 4. Reaction (ΔE_i) and activation (ΔE^{act}_i) energies for the three reaction mechanisms being studied (Eq.'s 3a, 3b, and 3c in Figure 2) on doubled doped surfaces. Site (5-Ir, 5-Co, or 5-Ni) indicates where the water molecule was initially adsorbed.

	F					s in eV			
Surface: Site	Direct Oxygen Recombination		O and OH Recombination			Associative			
	ΔE^{act}_{3a}	ΔE_{3a}	ΔE ^{act} _{3b}	ΔE_{3b}	$\Delta E_{3b.1}$	ΔE ^{act} _{3c}	ΔE _{3c}		
2xCo-IrO ₂ : 5-Ir	0.84	0.07	1.13	0.58	-0.52	0.74	0.40		
2xCo-IrO ₂ : 5-Co	0.84	0.62	1.39	1.30	-0.84	0.86	0.22		
2xNi-IrO ₂ : 5-Ir	0.38	-0.72	0.89	0.39	-0.68	0.63	0.29		
2xNi-IrO ₂ : 5-Ni	0.38	-0.13	0.79	0.69	-0.99	0.54	-0.66		

3.4. Experimental Comparison of NiIrO_x and CoIrO_x with IrO₂

To gain insight into the similarities and differences between cobalt and nickel interacting with iridium oxide, we compared the structure and intrinsic OER activities (i.e., mass and specific activity) and their stabilities of hydrous nickel-iridium oxide 2D nanoframes, hydrous cobalt-iridium oxide 2D nanoframes and compared these with commercial IrO₂. The as-prepared nickel-iridium 2D nanoframes are notated as "NiIr-CL", and the cobalt-iridium 2D nanoframes are notated as "CoIr-CL". The "CL" denotes that the materials have undergone a chemical leaching step, which was shown to remove unstable metals within our prior studies.³³,

Scanning electron microscopy (SEM) images of NiIr-CL and CoIr-CL (Figure 10a and b) show the materials have a nanostructured morphology which is composed of interconnected network of solid particles (2D nanoframe) and pores. Energy-dispersive x-ray spectroscopy (EDS) mapping images (Figure 10c and d) show that iridium, oxygen, and the non-noble metal, either nickel or cobalt, are well distributed within the structure, and their relative percent's were in line with values determined by inductively coupled plasma mass spectrometry (ICP-MS). ³³,

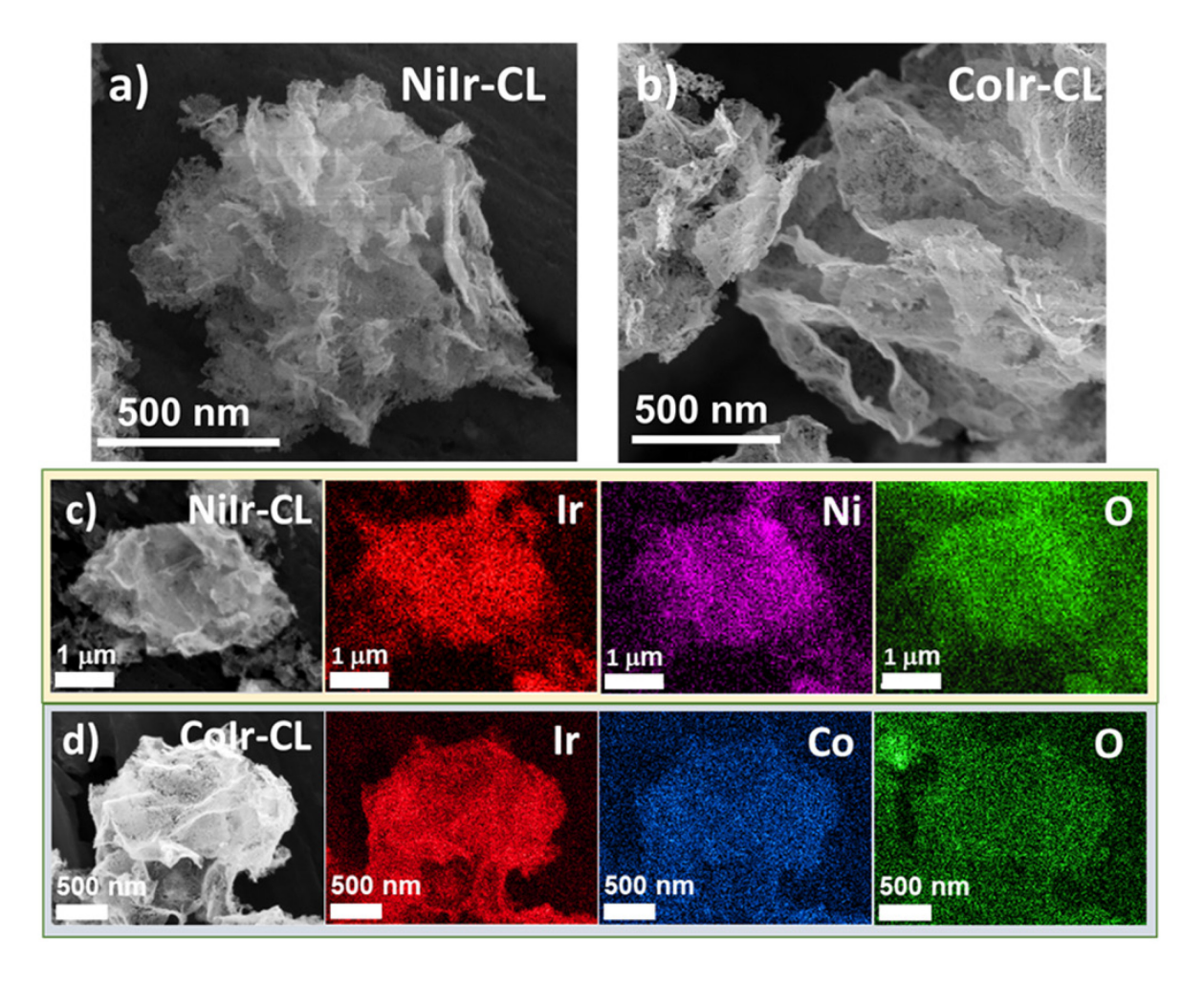


Figure 10. Comparison of morphology and composition of nickel-iridium (NiIr-CL) and cobalt-iridium (CoIr-CL) 2D nanoframes; scanning electron microscopy (SEM) images of NiIr-CL (a) and CoIr-CL (b); energy-dispersive x-ray spectroscopy (EDS) mapping images of NiIr-CL (c) and CoIr-CL (d) and showing distribution of iridium, cobalt or nickel, and oxygen within the structures (Adapted from ref. ³³ and reproduced with permission; copyright 2018, American Chemical Society; adapted from ref. ³⁴ and reproduced with permission; copyright 2021, Royal Society of Chemistry)

The comparison of cyclic voltammetry (CV) scans of hydrous nickel-iridium oxide 2D nanoframes (NiIr-CL-EO), hydrous cobalt-iridium oxide 2D nanoframes (CoIr-CL-EO), and commercial IrO₂ is shown in Figure 11. The CV scans were obtained after exposing the asprepared materials to an "electrochemical oxidation" step (notated with an "EO" subscript) comprising 60 scans between 0.05-1.5 V_{RHE}, which exposes the surface to OER potentials. In the region from 0.05 V to 1.0 V, the CV scans show two mains anodic (Ao and Bo) and cathode peaks (A_R and B_R) associated with oxidation and reduction, respectively, of surface iridium

hydroxide/oxide species. In particular, the CVs of NiIr-CL-EO and CoIr-CL-EO show an anodic peak, A₀, at a significantly lower potential of ~0.27 V_{RHE} for CoIr and ~0.42 V_{RHE} for NiIr compared to the voltage of the peak at IrO_{2,EO} (~0.48 V_{RHE}). For IrO_{2,EO}, the anodic peak at ~0.48 V_{RHE} (labeled A₀) has been attributed to formation of iridium (III) hydroxide⁵⁷ and modelled as the oxidation of two Ir³⁺-OH₂ groups to two Ir⁴⁺-OH groups,⁵⁸ and the peak at ~0.81 V (labeled B₀) has been attributed to oxidation of iridium (III) hydroxide to tetravalent IrO₂ or IrO(OH)₂.^{57, 59} The lower voltages of the A₀ peaks within NiIr-CL-EO and CoIr-CL-EO compared to IrO_{2,EO} suggest lower activation energy may be related to different local chemical environments for the hydrated Ir-OH species at the surface, in agreement with the electronic distribution effects illustrated in Figure 9 and activation energies (Table 1 and 3).

The importance of the environment of surface -OH groups is supported by prior studies that report iridium hydroxy (Ir-OH) surface species are strongly linked to OER activity, ⁶⁰ OH groups that act as reactive surface intermediates for the OER catalytic reaction, ⁶¹ and Ir-OH groups can be considered as descriptors for OER activity. ⁶² Indeed, as discussed in the above sections, the initial water oxidation steps are spontaneous on p-IrO₂ and generate OH groups adsorbed on 5-Ir sites, whereas H is adsorbed on O_b sites. Similar behavior was observed in the doped surfaces, although the easiness of the first water oxidation step was dependent on the amount of the dopant on the surface (Table 1 and Table 3). Note that the mechanism of the 1st water oxidation is similar in the doped surfaces, with OH adsorbing on the 5-Ir site and H on O_b with the doped element located on the 6-D sites. The presence of these adsorbed OH sites are crucial for the subsequent O₂ evolution steps. In relation to the electronic structure effects, it is useful to computationally analyze structures having large amounts of dopants on the surface to maximize the contribution of the dopant and determine its effects. As shown in Figure 9, we found a significant electron accumulation at the doped sites and depletion between the doped site and the surrounding O atoms. We emphasize that the dopant in the 6-D site

induces a strong accumulation of electron density around its proton acceptors neighboring O atoms which play a crucial role during the various OER electrochemical steps, as remarked in the above discussion of the reaction mechanisms.

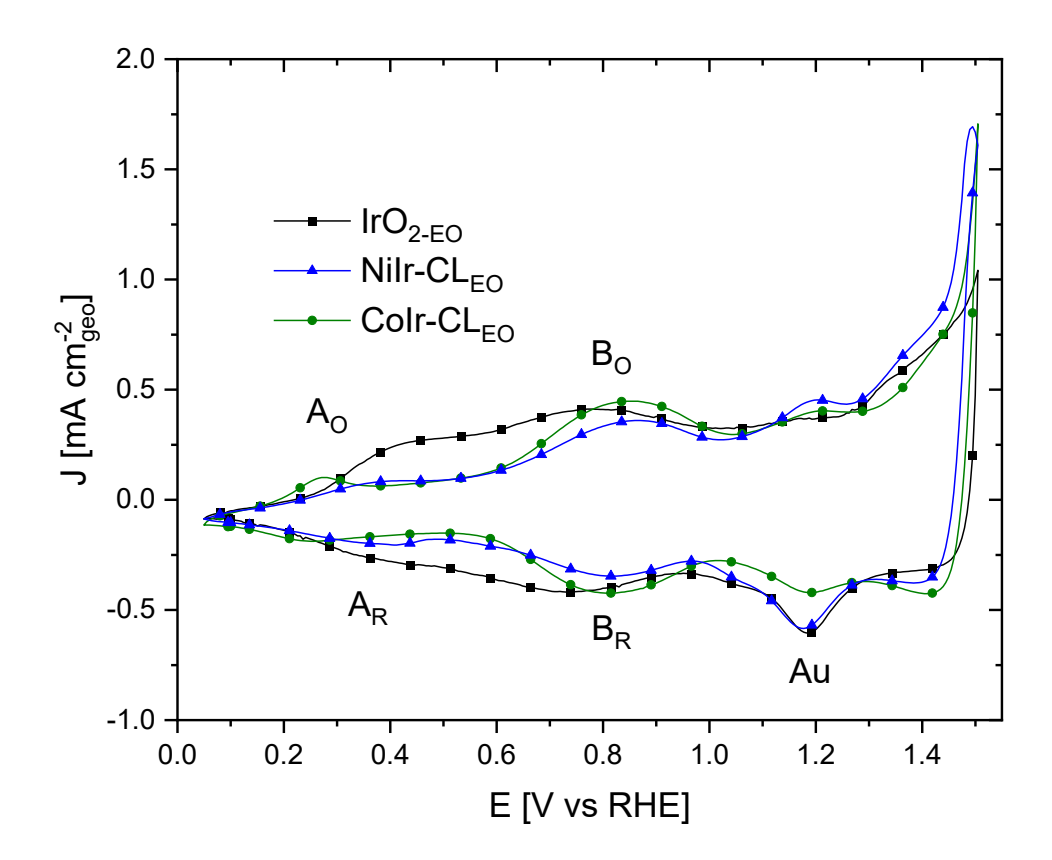


Figure 11. Comparison of cyclic voltammograms of CoIr-CL_{EO}, NiIr-CL_{EO}, and IrO_{2-EO} after electrochemical oxidation; peaks A and B are notated as oxidation (labelled with subscript "O") or reduction (labelled with subscript "R") peaks; the AuO_x reduction peak from the Au current collector is marked "Au" (Adapted from ref. ³³ and reproduced with permission; copyright 2018, American Chemical Society; adapted from ref. ³⁴ and reproduced with permission; copyright 2021, Royal Society of Chemistry).

The OER activity and stability were determined using thin-film rotating disk electrode measurements, using methods previously reported by our group. ^{33, 34} We determined the initial OER activity after electrochemical oxidation (notated with "EO"), and the OER activity after an accelerated durability testing protocol (notated with "ADT") that consisted of applying a constant potential of 1.6 V for 13.5 hours. The chronoamperometric polarization curves, normalized versus the mass of Ir, for CoIr-CL, NiIr-CL and IrO₂, after EO and after ADT are

shown in Figure 12a. The higher Ir mass-normalized currents observed for CoIr-CLEO and NiIr-CLEO within the OER chronoamperometric curves clearly showed a more efficient use of Ir during OER compared to IrO_{2.EO}. The higher mass activity is a combination of higher specific activity (discussed below) and the contribution of surface area of the CoIr-CLEO and NiIr-CLEO catalysts. 33,34 The mass-normalized OER activities of CoIr-CLEO, NiIr-CLEO and IrO2,EO were compared at 1.51 V_{RHE} and are shown in Figure 12c. At a potential of 1.51 V_{RHE}, the mass activities of CoIr-CL_{EO} ($243 \pm 47 \text{ A g}_{\text{Ir}}^{-1}$) and NiIr-CL_{EO} ($146 \pm 35 \text{ A g}_{\text{Ir}}^{-1}$) are 17 and 10 times higher than the mass activity of IrO_{2,EO} (14 ± 1 A g_{Ir}^{-1}). We also determined the specific activity by normalizing the current at 1.51 V_{RHE} to the electrochemical surface area determined by pseudocapacitance measurements.^{33, 34} The comparison of the specific activities of CoIr-CL_{EO}, NiIr-CL_{EO} and IrO_{2,EO} (Figure 12d) shows that CoIr-CL_{EO} and NiIr-CL_{EO} exhibit substantially higher specific activities compared to IrO_{2,EO}. The higher activities of CoIr-CL_{EO} and NiIr-CL_{EO} are attributed to the presence of highly active Ir-OH species that may interact with subsurface Co or Ni. Our prior studies of NiIr-CL and CoIr-CL using x-ray photoelectron spectroscopy showed that Ni and Co are within the surface region of the catalysts.^{33, 34} The presence of Co or Ni within the IrO₂ surface structure may modify the electron density distribution around the doped sites as supported by our computational analysis (Figure 9). The presence of doping elements, mainly on 6-coordinated sites, demonstrated an important impact on the electron density distribution, affecting principally the bridging oxygen atoms, which can serve as proton acceptors and increase the reactivity toward OER, although the effects are heavily dependent on the surface composition, as noted in the Discussion section below.

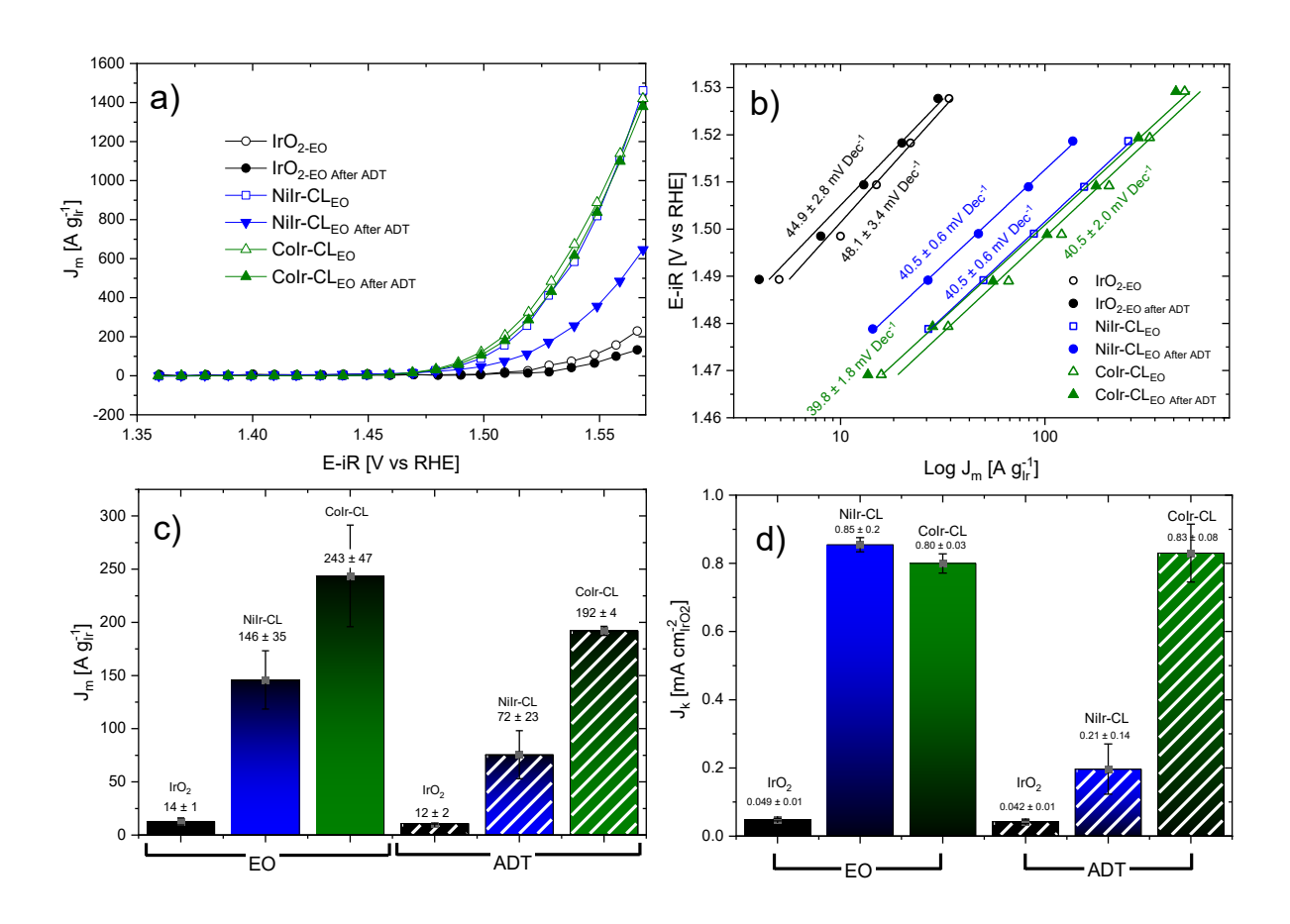


Figure 12. (a) Current in the oxygen evolution reaction (OER) voltage region determined from chronoamperometry measurements of CoIr-CL_{EO} 2D nanoframes, NiIr-CL_{EO} 2D nanoframes and commercial IrO₂ before and after accelerated durability testing (ADT) in O₂-free 0.1 M HClO₄. The stability was carried out using a potentiostatic procedure by holding the working electrode at 1.6 V_{RHE} iR-corrected for 13.5 hours under rotation at 2500 rpm; (b) Tafel slopes before and after accelerated durability testing determined by chronoamperometry using the iR-corrected potential; (c) comparison of OER mass activities at 1.51 V_{RHE} before and after accelerated durability testing; and (d) comparison of OER specific activities at 1.51 V_{RHE} before and after accelerated durability testing (Adapted from ref. ³³ and reproduced with permission; copyright 2018, American Chemical Society; adapted from ref. ³⁴ and reproduced with permission; copyright 2021, Royal Society of Chemistry).

Analysis of the Tafel slopes of CoIr-CL_{EO}, NiIr-CL_{EO}, and IrO_{2,EO} (Figure 12b) was performed to provide insight into the reaction mechanism. The Tafel slopes of CoIr-CL_{EO} $(40.5 \pm 2.0 \text{ mV dec}^{-1})$ and NiIr-CL_{EO} $(40.5 \pm 0.6 \text{ mV dec}^{-1})$ are similar to the Tafel slope of IrO_{2,EO} $(44.9 \pm 2.8 \text{ mV dec}^{-1})$. The similar Tafel slopes suggest similar reaction mechanistic pathways and a similar rate-determining step occurs within the oxygen evolution reaction pathway on the catalyst surface with the caveat that the coverage of adsorbed species may alter Tafel slopes.⁶³ This inference is in agreement with the theoretical results which reveal the same

mechanism and rate determining step (rds) for the pristine and doped surfaces, as detailed in the next section. The experimental Tafel slopes are in the range of ~40 mV dec⁻¹, which considering calculations of theoretical Tafel slopes (Table S6, ESI) suggests that the adsorption energies and kinetic barrier associated with the second oxidation stage of water (eq. III) would be the reaction limiting step. The comparison of the rds determined from the experimental Tafel slopes with the rds determined from DFT and factors involved with the predicted Tafel slopes are presented in the following Discussion section.

In addition to analysis of the Tafel slopes, we determined the activation energy, $\Delta G^{\#}$, of the rds building on prior work that established that the exchange current density, j_o , is correlated with activation energy of the reaction, $\Delta G^{\#}$.⁶⁴ The exchange current density is typically represented as a current normalized electrode geometrical area (i.e. A cm⁻²geo). Within nanomaterials, the effective catalyst area is much larger than the geometric area of the electrode, ⁶⁵ and therefore the exchange current density is also a function of the catalyst loading and catalyst specific surface area. Considering the nanostructured morphology (Figure 10) of our materials, we determined a specific exchange current density, $j_{o,s}$, which considers the loading and catalyst specific surface area, as represented by the following equation:

$$j_{0,s} = \frac{j_0}{L \cdot ECSA}$$
 3.4.1

where L is the catalyst loading (mg_{cat} cm⁻²_{geo}) and ECSA is the electrochemical surface area, (m² g⁻¹) determined from pseudocapacitive measurements.^{33, 34} Modifying the equation reported by Over et al.⁶⁴ for the specific exchange current density, we calculated $\Delta G^{\#}$ using equation below:

$$\Delta G^{\#} = -k_B T \cdot \ln \left(\frac{j_{0,s} \cdot h}{k_B T \cdot ze\Gamma_{act}} \right)$$
3.4.2

where k_B is Boltzmann's constant, T is absolute temperature in K, h is Planck's constant, z is number of electrons transferred in the reaction, and Γ_{act} is the number of electrocatalyst active

sites per surface area with an above reactant molecule or ion in the double layer. Considering this equation as describing a rate-determining step, we used z=1. For the value of Γ_{act} , we determined the area of the (110) IrO₂ slab used within our simulations of 41.317 Å² (Lattice a=6.396 Å and b=6.460 Å) and 2 active sites within this area; the sites per area is 0.048 sites/Å². Regarding the number of sites, the surface slab has 4 metallic sites exposed (two 5-Me and two 6-Me); however, the adsorption of water only takes place on the 5-Me sites since the adsorption energy on 6-Me sites is very weak or non-favorable. There are also 2 oxygen atoms that act as proton acceptors, which are affected by the 6-coordinated metallic sites. The values for the specific exchange current density and activation energy for IrO_{2-EO}, NiIr-CL_{EO}, and CoIr-CL_{EO} are shown in Table 5. From our calculations, IrO_{2-EO} has a higher activation energy compared to NiIr-CL_{EO} and CoIr-CL_{EO}, and NiIr-CL_{EO} has a slightly lower activation energy than CoIr-CL_{EO}. The calculated values of $\Delta G^{\#}$ are in good agreement with the OER specific activities (Figure 12): lower activation energy correlates with higher specific activity.

Table 5. Comparison of specific exchange current density and calculated activation energy for IrO₂-EO, NiIr-CLEO, and CoIr-CLEO.

Material	Specific exchange current density, j _{0,s} (mA cm ⁻² _{IrO2})	Activation energy, $\Delta G^{\#}(eV)$	
IrO ₂ -EO	1.12×10^{-8}	1.17	
NiIr-CLEO	1.93×10^{-6}	1.04	
CoIr-CL _{EO}	2.65×10^{-6}	1.09	

We next compared the stability of the CoIr-CL and NiIr-CL nanoframes. While the CoIr-CL and NiIr-CL nanoframes showed similar initial OER activity, the stability was significantly different between the materials. The comparison of the iridium mass-normalized current, Tafel slopes, OER mass activities, and OER specific activities of CoIr-CL_{ADT}, NiIr-CL_{ADT} and IrO_{2-ADT} (after ADT) are presented in Figure 12a-d. The mass activities were corrected for dissolution of iridium. The Tafel slopes for the catalysts remained relatively

similar before and after ADT (Figure 12b), suggesting similar reaction mechanisms before and after ADT. For IrO₂, the OER mass activity (Figure 12c) and specific activity (Figure 12d) decreased after the durability testing. For NiIr-CL and CoIr-CL after ADT, the two materials showed vastly different stabilities. The mass activity and specific activity of the NiIr catalyst decreased significantly after ADT. However, for CoIr-CL the specific activity remained similar after ADT, which translates into a higher mass activity retention of ~78 % after ADT which was significantly higher than the value for NiIr-CL nanoframes of 25%.

The NiIr-CL and CoIr-CL nanoframes show structural differences that may contribute to observed different stabilities. The presence of cobalt oxides within CoIr-CL even after acid leaching was supported by XRD and XPS analysis; ³⁴ in contrast, nickel oxides were not clearly observed after thermal treatment at 300 °C in hydrogen and acid leaching. ³³ The cobalt-containing CoIr-CL nanoframes also did not show a clearly defined metallic alloy phase after thermal reduction in hydrogen, ³⁴ in contrast to the nickel-containing NiIr-CL nanoframes. ³³ Considering their similar morphologies and structures, these electrochemical stability differences may be related to a stronger Ir-O-Co interaction in comparison with Ir-O-Ni. A prior computational analysis has demonstrated a higher relative formation energy toward Co-doped IrO₂ structure compared with Ni-doped IrO₂, ⁶⁰ which may contribute to the enhanced stability of CoIr-CL compared with NiIr-CL. In addition, the calculated results shown in Figure S2 indicate that the O-Co interactions are stronger than those of O-Ni which may suggest that the Ir-O-Co could be also a stronger interaction than the corresponding for Ni, considering that the Ir-O interaction is similar for both doped systems.

3.5. Discussion

Overall, from our theoretical analysis, the presence of Ni or Co atoms within the surfaces of IrO₂ improved the energetics of reactions both thermodynamics and kinetics when compared with the pristine metal oxide. Co-doping is found to yield better results than Ni-

doping for substituting penta-coordinated sites on the first two electrochemical steps (Eq. 1 and 2, Figure 2). On the other hand, Ni-doping is more impactful on the formation of the OOH on the associative mechanism as well as on non-electrochemical steps. The impact on the non-electrochemical steps (Eq. 3a and 3b, Figure 2) is most likely due to the difference in adsorption energies. Similar behavior is found from single or double-doped IrO₂ electrocatalysts. When the doping is performed on hexa-coordinated sites, the presence of Ni and Co yields a substantial improvement on the energies of reaction and activation for electrochemical steps, i.e., reactions involving proton transfer (Eq. 1, 2, 3b.1, and 3c, Figure 2). However, the energetics of reaction are comparable or worsen for recombination reactions (non-electrochemical steps: Eq. 3a and 3b, Figure 2) when compared to those obtained from the pristine electrode surface.

In order to determine the rate determining step (rds) from the DFT calculations, the activation energies of the multiple reactions steps are summarized and tabulated in Table 6 and Table 7 for comparison.

Table 6. Summary of activation (ΔE^{act}_i) energies for Eq. 1, 2, 3a, 3b, and 3c in Figure 2 on pristine or single Co- or Ni-doped IrO₂ surfaces. Results from pristine and Co-doped IrO₂ and Ni-doped IrO₂ surfaces are taken from Tables 1, S1, S2, and S3 and are summarized here for comparison purposes. Site (5-Ir, 5-Co, or 5-Ni) indicates where the water molecule was initially adsorbed. Underlined values identify those steps where no transition state was found, and the endothermic reaction energy is tabulated instead. Italicized and bolded values represent the activation energy for the rate determining step for each of the modeled systems. *Electrochemical steps.

Surface: Site	Activation Energies in eV					
	ΔE ^{act} 1 [#]	ΔE ^{act} 2 [#]	ΛE ^{act} 3a	ΔE ^{act} 3b	ΔE ^{act} 3c [#]	
p-IrO ₂ : 5-Ir	-	0.56	0.82	1.53	0.66	
5Co-IrO ₂ : 5-Ir	-	0.48	0.85	1.01	0.70	
5Co-IrO ₂ : 5-Co	0.20	0.47	0.85	1.42	0.92	
6Co-IrO ₂ : 5-Ir	-	0.45	1.03	1.64	0.54	
5Ni-IrO ₂ : 5-Ir	-	0.81	0.38	0.77	0.66	
5Ni-IrO ₂ : 5-Ni	0.29	0.74	0.37	0.68	0.51	
6Ni-IrO ₂ : 5-Ir	-	0.38	0.91	1.50	0.59	

Table 7. Summary of activation (ΔE^{act}_i) energies for Eq. 1, 2, 3a, 3b, and 3c in Figure 2 on double Coor Ni-doped IrO₂ surfaces. Results from double doped IrO₂ surfaces are taken from Tables 3 and 4 and are summarized here for comparison purposes. Site (5-Ir, 5-Co, or 5-Ni) indicates where the water molecule was initially adsorbed. Underlined values identify those steps where no transition state was found, and the endothermic reaction energy is tabulated instead. Italicized and bolded values represent the activation energy for the rate determining step for each of the modeled systems. *Electrochemical steps.

Surface: Site	Activation Energies in eV					
	$\Delta { m E}^{ m act}{}_1{}^{\#}$	$\Delta { m E}^{ m act}{}_2{}^{\#}$	ΔE ^{act} 3a	$\Delta \mathrm{E}^{\mathrm{act}}$ 3b	$\Delta E^{act}_{3c}^{\#}$	
2xCo-IrO ₂ : 5-Ir	-	0.47	0.84	1.13	0.74	
2xCo-IrO ₂ : 5-Co	0.06	0.36	0.84	1.39	0.86	
2xNi-IrO ₂ : 5-Ir	-	0.58	0.38	0.89	0.63	
2xNi-IrO ₂ : 5-Ni	0.10	0.56	0.38	0.79	0.54	

From the results, the direct oxygen recombination by reaction of two O* adsorbed species (non-electrochemical) is very unlikely in most surfaces, except for 5-Ni doped surface (Figure 6 and Table 4) where this step is predicted to be favorable. The alternative route requires formation of HOO* (non-electrochemical, eq. 3b, or electrochemical, eq. 3c/3c'), and although more favorable than the direct oxygen recombination, it is the least favorable step in the complete reaction scheme (i.e., the rds) for each case. Table 6 and Table 7 clearly show that the associative mechanism (electrochemical reaction 3c/3c'), where a water molecule from the liquid phase acts as proton donor and acceptor leading to the HOO* and H# adsorbed species, is the most likely scenario on the pristine and doped surfaces. On the Co-doped surfaces, the best configuration for this step was found for Co on the 6D, with 5-Ir for the active site. In contrast, on the Ni surface, Ni substituted on the 5D, and the 5-Ni site performs best for this step. It is important to notice that, in this case, the activation energy of the second electrochemical step (eq. 2) could be higher than that of the equation 3c depending on the concentration of the dopant on the surface and the active site (see values in bold for $\Delta E^{act}_2^{\#}$ in Table 6 and Table 7). If we considered this and the lower activation barriers for the oxygen recombination steps, either the direct oxygen recombination or associative mechanism could take place on Ni-doped surface and the preferential mechanism will depend on the sites being substituted and the active sites on the surface of the electrocatalyst.

To allow comparison of the rate determining step (rds) from calculations and experiments, we first compared the experimental Tafel slopes to the predicted Tafel slopes for the different mechanistic steps. The experimental Tafel slopes for the Ni- and Co-doped IrO₂ and pristine IrO₂ are within the range of 40-45 mV dec⁻¹ (Figure 12b) which suggests that the reaction proceeds via similar pathways on pristine and doped IrO₂ surfaces. Theoretically predicted Tafel slopes considering each of the mechanism steps as the anodic rds were calculated using the following equation

$$b = \frac{dE}{d\log j_a} = \frac{2.303 RT}{\alpha_a F}$$
3.5.1

where b is the Tafel slope, E is the potential, j_a is the anodic current density, R is the gas constant, E is temperature, E is the anodic transfer coefficient, and E is Faraday's constant. E is E is Faraday's constant. E is E is Faraday's constant. E is the gas constant, E is the anodic transfer coefficient was calculated using the following equation

$$\alpha_a = \frac{n_f}{n} + n_r \beta$$
 3.5.2

where n_f is the number of electrons transferred before the rds, v is the number of occurrences of the rds in the electrode reaction (in this case, v=1), n_r is the number of electrons transferred during the rate determining step, and β is the symmetry factor (usually assumed to take values close to 0.5).⁶⁶ For each of the three mechanisms considered from our DFT analysis (Associative mechanism, Direct oxygen recombination mechanism, and O and OH Recombination Mechanism), we calculated the theoretically predicted Tafel slopes for each of the different reaction steps as the rds, as presented in Table S6, ESI. Using a value of $\beta=0.5$, the 2nd oxidation step (equation III) has a theoretical Tafel slope of 40 mV dec⁻¹ which is similar to the values of experimentally measured Tafel slopes of 40-45 mV dec⁻¹ which would support

that from this analysis that the 2nd oxidation step is the rds. In contrast, our DFT analysis indicates that for most cases the HOO* formation step described by equation IV is the rds which has a predicted Tafel slope of 25 mV dec⁻¹ (Table S6, ESI) from the current analysis.

The apparent difference between the rds determined from experiments and DFT calculations using the predicted Tafel slopes suggests additional factors are involved and need to be further included to enable agreement between theory and experiment of the rds. The analysis used for the predicted Tafel slopes assumes a symmetric potential energy barrier $(\beta=0.5)^{55}$ and does not consider the contribution of adsorbed species, possible rearrangements of reaction site(s), and the influence of the electrolyte. There are different models and interpretations of the meaning of the symmetry factor with no generally agreed upon consensus. 66,67 Large deviations from β =0.5 are predicted when the reactant and product force constants are different and if the reactant exchanges an electron with the metal while being in the adsorbed state. 66 The relative contributions of enthalpic and entropic components can also influence the value of β . ^{68, 69} In addition to factors affecting the symmetry factor, microkinetic analysis supports that changes of the coverage of adsorbed species, which were not considered here, may alter Tafel slopes. 63 Tafel slopes can also be influenced by rearrangement as suggested by the OER on RuO₂.^{70, 71} 69, 70 The water structure and/or solvation properties of the ions in the electrolyte also alters the OER kinetics.⁷² 71 Additionally, we note that there are structural differences (edge sites, contribution of a less ordered/amorphous IrOx surface layer, etc.) between the structure used for theoretical analysis and the experimentally determined structure that can affect the comparison.

It is evident that modeling and experimental analysis of such a complex and continuously evolving surface is far from trivial, and additional work is needed before we can provide a conclusive statement from both theory and experiment with respect to the rds. However, the value of the activation energies $\Delta G^{\#}$ calculated from the exchange current density

is in the range of the values predicted from DFT, and from these values NiIr-CL and CoIr-CL have lower activation energies compared to IrO₂. Our theoretical analysis provides additional insights about the role of the dopants on facilitating the OER, and about the nature of the active sites. The comparison with the experimental activities suggests what surface configurations would optimize the catalytic performance. Further work is needed to bridge the gap that would allow a better integration between theory and experiments. On the experimental side, further surface characterization would be useful to distinguish possible mechanisms, particularly to determine the presence of surface HOO* species that occur in the mechanistic steps of Eq. 3b, but not Eq. 3a. On the theoretical side, understanding metal dissolution effects and the evolution of the catalyst surface under reaction conditions are challenges that need to be addressed in future studies. In addition, the importance of ab initio simulations at constant potential have been demonstrated³² and combined with microkinetic modeling shown to provide further realistic insights. Moreover, a model based on constrained-ab initio molecular dynamics⁷³ 72 would be particularly useful for incorporating solvation effects and characterizing protonation and deprotonation steps as well as solvation of intermediate species, and also to evaluate metal dissolution reactions.⁷⁴ 73Representative hydroxyl surface coverage as determined by ab initio thermodynamics modeling of the surrounding environment⁵³ as a function of acidic medium and applied potential is another important point toward a more accurate model.

4. Conclusions

We evaluated the effects of cobalt and nickel-doping within IrO₂ on the oxygen evolution reaction using calculations and experiments. Our DFT calculations show that the metal dopant affects the distribution of electronic charge and affects the thermodynamics and kinetics aspects of the OER when compared with undoped, pristine IrO₂. When Ni or Co is

present within IrO₂, the activation energies are lowered and the reaction energies become more exothermic. The effect of the dopant is dependent on the location of the dopant species within the surface layer, and dopants affect the adsorption of the intermediates directly onto the dopant metal or the neighboring sites. The comparison of three different pathways on how the O-O bond is formed shows that the associative mechanism, where a water molecule from the liquid phase acts as proton donor and acceptor leading to the HOO* and H# adsorbed species, is the most likely scenario on the pristine and doped surfaces. The comparison of the distribution of electronic charges for the pristine and doped surfaces for the three different pathways clarifies why the associative mechanism is preferred for the O₂ formation, since it avoids the repulsive interaction between the two highly charged adsorbed O atoms. The direct oxygen recombination by reaction of two O* adsorbed species is very unlikely in most cases, except for 5-Ni doped surface, where this step is predicted to be favorable. For the case of the Nidoped surface, the preferred mechanism may depend on the sites being substituted and the active sites on the surface of the electrocatalyst. Therefore, our DFT calculations show that the metal dopant can in some cases affect not only the reaction rate but the preferred reaction mechanism as well.

The activation energies calculated from exchange current densities were lower for Ni and Co-doped IrO₂ compared to undoped IrO₂, which is in good agreement with the theory. From the Tafel slopes determined experimentally, we concluded that there is a unique mechanism for the pristine and doped surfaces. The apparent difference between the rds determined from experiments and DFT calculations using the predicted Tafel slopes suggests the predicted Tafel slopes do not fully account for the multiple factors involved in the reaction, and additional studies are needed to connect experiment and theory in regard to the rds. In addition to the effect on OER activity, Ni or Co within IrO₂ was determined to also affect the stability with Co providing a significantly better stability compared with Ni which may be due

to a higher metal-oxygen bond strength within the Co-containing material. Understanding the effect of doping within IrO₂ furthers our ability to design materials with enhanced OER performance that result in improved water electrolyzers and other electrolysis processes.

Acknowledgments

The authors acknowledge support of this research from the National Science Foundation Award No. 1936458 and 1936495. P.B.B, G.R.S, and L.E.C.F gratefully acknowledge supercomputer resources from the Texas A&M University High Performance Computer Center and Texas Advanced Computing Center (TACC).

Supporting Information

Bond distance time-evolution obtained from AIMD simulations (Fig. S1 and S3), OH and O adsorption energies on doped sites of IrO₂ surfaces (Fig. S2), raw data for reaction and activation energies (Tables S1-S3), time to first oxidation step of water (from AIMD simulations) on double doped IrO₂ systems (Table S5), and predicted Tafel slopes for oxygen evolution reaction step (Table S6).

References

- 1. Hanna, M. C.; Nozik, A. J., Solar conversion efficiency of photovoltaic and photoelectrolysis cells with carrier multiplication absorbers. *J. Appl. Phys.* **2006**, *100* (7).
- 2. Garcia-Mota, M.; Vojvodic, A.; Metiu, H.; Man, I. C.; Su, H. Y.; Rossmeisl, J.; Norskov, J. K., Tailoring the Activity for Oxygen Evolution Electrocatalysis on Rutile TiO(2)(110) by Transition-Metal Substitution. *ChemCatChem* **2011**, *3* (10), 1607-1611.
- 3. Pivovar, B. *Current Status of Electrolyzer Technology and Needs for Successful Widespread Commercialization and Meeting Hydrogen Shot Targets*; National Renewable Energy Laboratory: U.S. Department of Energy (DOE) Hydrogen Shot Summit, August 31, 2021.
- 4. Petrykin, V.; Macounová, K.; Okube, M.; Mukerjee, S.; Krtil, P., Local structure of Co doped RuO2 nanocrystalline electrocatalytic materials for chlorine and oxygen evolution. *Catalysis Today* **2013**, *202*, 63-69.
- 5. Petrykin, V.; Macounova, K.; Franc, J.; Shlyakhtin, O.; Klementova, M.; Mukerjee, S.; Krtil, P., Zn-Doped RuO2 electrocatalyts for Selective Oxygen Evolution: Relationship between Local Structure and Electrocatalytic Behavior in Chloride Containing Media. *Chemistry of Materials* **2011**, 23 (2), 200-207.

- 6. Niishiro, R.; Konta, R.; Kato, H.; Chun, W.-J.; Asakura, K.; Kudo, A., Photocatalytic O2 Evolution of Rhodium and Antimony-Codoped Rutile-Type TiO2 under Visible Light Irradiation. *The Journal of Physical Chemistry C* **2007**, *111* (46), 17420-17426.
- 7. Li, B. B.; Liang, Y. Q.; Yang, X. J.; Cui, Z. D.; Qiao, S. Z.; Zhu, S. L.; Li, Z. Y.; Yin, K., MoO2-CoO coupled with a macroporous carbon hybrid electrocatalyst for highly efficient oxygen evolution. *Nanoscale* **2015**, *7* (40), 16704-16714.
- 8. Li, M.; Zhang, L.; Xu, Q.; Niu, J.; Xia, Z., N-doped graphene as catalysts for oxygen reduction and oxygen evolution reactions: Theoretical considerations. *Journal of Catalysis* **2014**, *314*, 66-72.
- 9. Valdés, Á.; Qu, Z. W.; Kroes, G. J.; Rossmeisl, J.; Nørskov, J. K., Oxidation and Photo-Oxidation of Water on TiO2 Surface. *The Journal of Physical Chemistry C* **2008**, *112* (26), 9872-9879.
- 10. Reier, T.; Nong, H. N.; Teschner, D.; Schlögl, R.; Strasser, P., Electrocatalytic Oxygen Evolution Reaction in Acidic Environments Reaction Mechanisms and Catalysts. *Adv. Energy Mater.* **2017,** *7* (1), 1601275.
- 11. Carmo, M.; Fritz, D. L.; Mergel, J.; Stolten, D., A Comprehensive Review on PEM Water Electrolysis. *Int. J. Hydrogen Energ.* **2013**, *38* (12), 4901-4934.
- 12. Alia, S. M.; Rasimick, B.; Ngo, C.; Neyerlin, K. C.; Kocha, S. S.; Pylypenko, S.; Xu, H.; Pivovar, B. S., Activity and Durability of Iridium Nanoparticles in the Oxygen Evolution Reaction. *J. Electrochem. Soc.* **2016**, *163* (11), F3105-F3112.
- 13. GreeleyJ; Stephens, I. E. L.; Bondarenko, A. S.; Johansson, T. P.; Hansen, H. A.; Jaramillo, T. F.; RossmeislJ; Chorkendorffl; Nørskov, J. K., Alloys of platinum and early transition metals as oxygen reduction electrocatalysts. *Nat Chem* **2009**, *1* (7), 552-556.
- 14. Fuentes, R. E.; Farell, J.; Weidner, J. W., Multimetallic Electrocatalysts of Pt, Ru, and Ir Supported on Anatase and Rutile TiO2 for Oxygen Evolution in an Acid Environment. *Electrochemical and Solid-State Letters* **2011**, *14* (3), E5-E7.
- 15. Chen, J.; Selloni, A., First Principles Study of Cobalt (Hydr)oxides under Electrochemical Conditions. *The Journal of Physical Chemistry C* **2013**, *117* (39), 20002-20006.
- 16. Mom, R. V.; Cheng, J.; Koper, M. T. M.; Sprik, M., Modeling the Oxygen Evolution Reaction on Metal Oxides: The Influence of Unrestricted DFT Calculations. *The Journal of Physical Chemistry C* **2014**, *118* (8), 4095-4102.
- 17. Suen, N. T.; Hung, S. F.; Quan, Q.; Zhang, N.; Xu, Y. J.; Chen, H. M., Electrocatalysis for the oxygen evolution reaction: recent development and future perspectives. *Chemical Society Reviews* **2017**, *46* (2), 337-365.
- 18. Rossmeisl, J.; Qu, Z. W.; Zhu, H.; Kroes, G. J.; Nørskov, J. K., Electrolysis of water on oxide surfaces. *Journal of Electroanalytical Chemistry* **2007**, *607* (1), 83-89.
- 19. Doyle, R. L.; Lyons, M. E. G., The Oxygen Evolution Reaction: Mechanistic Concepts and Catalyst Design. In *Photoelectrochemical Solar Fuel Production: From Basic Principles to Advanced Devices*, Giménez, S.; Bisquert, J., Eds. Springer International Publishing: Cham, 2016; pp 41-104.
- 20. Chen, Z. J.; Duan, X. G.; Wei, W.; Wang, S. B.; Ni, B. J., Iridium-based nanomaterials for electrochemical water splitting. *Nano Energy* **2020**, *78*, 28.
- 21. Shi, Q. R.; Zhu, C. Z.; Du, D.; Lin, Y. H., Robust noble metal-based electrocatalysts for oxygen evolution reaction. *Chemical Society Reviews* **2019**, *48* (12), 3181-3192.
- 22. Song, J. J.; Wei, C.; Huang, Z. F.; Liu, C. T.; Zeng, L.; Wang, X.; Xu, Z. C. J., A review on fundamentals for designing oxygen evolution electrocatalysts. *Chemical Society Reviews* **2020**, *49* (7), 2196-2214.
- 23. Man, I. C.; Su, H. Y.; Calle Vallejo, F.; Hansen, H. A.; Martínez, J. I.; Inoglu, N. G.; Kitchin, J.; Jaramillo, T. F.; Nørskov, J. K.; Rossmeisl, J., Universality in Oxygen Evolution Electrocatalysis on Oxide Surfaces. *ChemCatChem* **2011**, *3* (7), 1159-1165.
- 24. Rao, R. R.; Kolb, M. J.; Halck, N. B.; Pedersen, A. F.; Mehta, A.; You, H.; Stoerzinger, K. A.; Feng, Z.; Hansen, H. A.; Zhou, H.; Giordano, L.; Rossmeisl, J.; Vegge, T.; Chorkendorff, I.; Stephens, I. E. L.; Shao-Horn, Y., Towards identifying the active sites on RuO2(110) in catalyzing oxygen evolution. *Energy & Environmental Science* **2017**, *10* (12), 2626-2637.

- 25. Wohlfahrt-Mehrens, M.; Heitbaum, J., Oxygen evolution on Ru and RuO2 electrodes studied using isotope labelling and on-line mass spectrometry. *Journal of Electroanalytical Chemistry and Interfacial Electrochemistry* **1987**, *237* (2), 251-260.
- 26. Stoerzinger, K. A.; Diaz-Morales, O.; Kolb, M.; Rao, R. R.; Frydendal, R.; Qiao, L.; Wang, X. R.; Halck, N. B.; Rossmeisl, J.; Hansen, H. A.; Vegge, T.; Stephens, I. E. L.; Koper, M. T. M.; Shao-Horn, Y., Orientation-Dependent Oxygen Evolution on RuO2 without Lattice Exchange. *ACS Energy Letters* **2017**, *2* (4), 876-881.
- 27. González, D.; Heras-Domingo, J.; Pantaleone, S.; Rimola, A.; Rodríguez-Santiago, L.; Solans-Monfort, X.; Sodupe, M., Water Adsorption on MO2 (M = Ti, Ru, and Ir) Surfaces. Importance of Octahedral Distortion and Cooperative Effects. *ACS Omega* **2019**, *4* (2), 2989-2999.
- 28. Frydendal, R.; Paoli, E. A.; Chorkendorff, I.; Rossmeisl, J.; Stephens, I. E. L., Toward an Active and Stable Catalyst for Oxygen Evolution in Acidic Media: Ti-Stabilized MnO2. *Advanced Energy Materials* **2015**, *5* (22), 1500991.
- 29. Roy, C.; Rao, R. R.; Stoerzinger, K. A.; Hwang, J.; Rossmeisl, J.; Chorkendorff, I.; Shao-Horn, Y.; Stephens, I. E. L., Trends in Activity and Dissolution on RuO2 under Oxygen Evolution Conditions: Particles versus Well-Defined Extended Surfaces. *Acs Energy Letters* **2018**, *3* (9), 2045-2051.
- 30. Lee, H.; Kim, J. Y.; Lee, S. Y.; Hong, J. A.; Kim, N.; Baik, J.; Hwang, Y. J., Comparative study of catalytic activities among transition metal-doped IrO2 nanoparticles. *Scientific Reports* **2018**, *8* (1), 16777.
- 31. González-Huerta, R. G.; Ramos-Sánchez, G.; Balbuena, P. B., Oxygen evolution in Co-doped RuO2 and IrO2: Experimental and theoretical insights to diminish electrolysis overpotential. *Journal of Power Sources* **2014**, *268*, 69-76.
- 32. Ping, Y.; Nielsen, R. J.; Goddard, W. A., 3rd, The Reaction Mechanism with Free Energy Barriers at Constant Potentials for the Oxygen Evolution Reaction at the IrO(2) (110) Surface. *J Am Chem Soc* **2017**, *139* (1), 149-155.
- 33. Godínez-Salomón, F.; Albiter, L.; Alia, S. M.; Pivovar, B. S.; Camacho-Forero, L. E.; Balbuena, P. B.; Mendoza-Cruz, R.; Arellano-Jimenez, M. J.; Rhodes, C. P., Self-Supported Hydrous Iridium—Nickel Oxide Two-Dimensional Nanoframes for High Activity Oxygen Evolution Electrocatalysts. *ACS Catalysis* **2018**, *8* (11), 10498-10520.
- 34. Ying, Y. F.; Salomon, J. F. G.; Lartundo-Rojas, L.; Moreno, A.; Meyer, R.; Damin, C. A.; Rhodes, C. P., Hydrous cobalt-iridium oxide two-dimensional nanoframes: insights into activity and stability of bimetallic acidic oxygen evolution electrocatalysts. *Nanoscale Adv.* **2021**, *3* (7), 1976-1996.
- 35. Kresse, G.; Hafner, J., Ab initio molecular dynamics for liquid metals. *Physical Review B* **1993**, 47 (1), 558-561.
- 36. Kresse, G.; Hafner, J., Ab initio molecular-dynamics simulation of the liquid-metalamorphous- semiconductor transition in germanium. *Physical Review B* **1994**, *49* (20), 14251-14269.
- 37. Kresse, G.; Furthmuller, J., Efficiency of ab-initio total energy calculations for metals and semiconductors using a plane-wave basis set. *Computational Materials Science* **1996**, *6* (1), 15-50.
- 38. Blöchl, P. E., Projector augmented-wave method. *Physical Review B* **1994**, *50* (24), 17953-17979.
- 39. Kresse, G.; Joubert, D., From ultrasoft pseudopotentials to the projector augmented-wave method. *Physical Review B Condensed Matter and Materials Physics* **1999**, *59* (3), 1758-1775.
- 40. Hammer, B.; Hansen, L. B.; Nørskov, J. K., Improved adsorption energetics within density-functional theory using revised Perdew-Burke-Ernzerhof functionals. *Physical Review B Condensed Matter and Materials Physics* **1999**, *59* (11), 7413-7421.
- 41. Monkhorst, H. J.; Pack, J. D., Special points for Brillouin-zone integrations. *Phys. Rev. B* **1976**, *13* (12), 5188-5192.

- 42. Henkelman, G.; Jónsson, H., Improved tangent estimate in the nudged elastic band method for finding minimum energy paths and saddle points. *Journal of Chemical Physics* **2000**, *113* (22), 9978-9985.
- 43. Henkelman, G.; Uberuaga, B. P.; Jónsson, H., Climbing image nudged elastic band method for finding saddle points and minimum energy paths. *Journal of Chemical Physics* **2000**, *113* (22), 9901-9904.
- 44. Sheppard, D.; Terrell, R.; Henkelman, G., Optimization methods for finding minimum energy paths. *Journal of Chemical Physics* **2008**, *128* (13).
- 45. Tang, W.; Sanville, E.; Henkelman, G., A grid-based Bader analysis algorithm without lattice bias. *Journal of Physics Condensed Matter* **2009**, *21* (8).
- 46. Sanville, E.; Kenny, S. D.; Smith, R.; Henkelman, G., Improved grid-based algorithm for Bader charge allocation. *Journal of Computational Chemistry* **2007**, *28* (5), 899-908.
- 47. Henkelman, G.; Arnaldsson, A.; Jónsson, H., A fast and robust algorithm for Bader decomposition of charge density. *Computational Materials Science* **2006**, *36* (3), 354-360.
- 48. Matz, O.; Calatayud, M., Periodic DFT Study of Rutile IrO2: Surface Reactivity and Catechol Adsorption. *The Journal of Physical Chemistry C* **2017**, *121* (24), 13135-13143.
- 49. Sen, F. G.; Kinaci, A.; Narayanan, B.; Gray, S. K.; Davis, M. J.; Sankaranarayanan, S. K. R. S.; Chan, M. K. Y., Towards accurate prediction of catalytic activity in IrO2 nanoclusters via first principles-based variable charge force field. *Journal of Materials Chemistry A* **2015**, *3* (37), 18970-18982.
- 50. Gauthier, J. A.; Dickens, C. F.; Chen, L. D.; Doyle, A. D.; Nørskov, J. K., Solvation Effects for Oxygen Evolution Reaction Catalysis on IrO2(110). *The Journal of Physical Chemistry C* **2017**, *121* (21), 11455-11463.
- 51. BIOVIA Materials Studio 2016, 16.1.0.21; Dassault Systèmes BIOVIA: San Diego, 2015.
- 52. Zhao, S.; Yu, H.; Maric, R.; Danilovic, N.; Capuano, C. B.; Ayers, K. E.; Mustain, W. E., Calculating the Electrochemically Active Surface Area of Iridium Oxide in Operating Proton Exchange Membrane Electrolyzers. *J. Electrochem. Soc.* **2015**, *162* (12), F1292-F1298.
- 53. Sun, Q.; Reuter, K.; Scheffler, M., Effect of a humid environment on the surface structure of \${\mathrm{RuO}} {2}(110)\$. *Physical Review B* **2003**, *67* (20), 205424.
- 54. Ping, Y.; Nielsen, R. J.; Goddard, W. A., The Reaction Mechanism with Free Energy Barriers at Constant Potentials for the Oxygen Evolution Reaction at the IrO2 (110) Surface. *Journal of the American Chemical Society* **2017**, *139* (1), 149-155.
- 55. Li, T.; Balbuena, P. B., Computational Studies of the Interactions of Oxygen with Platinum Clusters. *The Journal of Physical Chemistry B* **2001**, *105* (41), 9943-9952.
- 56. Camacho-Forero, L. E. Estudio Computacional de la Evolución de Oxigeno sobre Óxidos Metálicos y sus Dopados. Bachelor's thesis, Universidad Industrial de Santander, UIS, Bucaramanga, 2014.
- 57. Kötz, R.; Neff, H.; Stucki, S., Anodic Iridium Oxide Films: XPS Studies of Oxidation State Changes and O₂ Evolution. *J. Electrochem. Soc.* **1984**, *131* (1), 72-77.
- 58. Steegstra, P.; Busch, M.; Panas, I.; Ahlberg, E., Revisiting the Redox Properties of Hydrous Iridium Oxide Films in the Context of Oxygen Evolution. *J. Phys. Chem. C* **2013**, *117* (40), 20975-20981.
- 59. Cherevko, S.; Geiger, S.; Kasian, O.; Mingers, A.; Mayrhofer, K. J. J., Oxygen Evolution Activity and Stability of Iridium in Acidic Media. Part 2. Electrochemically Grown Hydrous Iridium Oxide. *J. Electroanal. Chem.* **2016**, *774*, 102-110.
- 60. Abbott, D. F.; Lebedev, D.; Waltar, K.; Povia, M.; Nachtegaal, M.; Fabbri, E.; Copéret, C.; Schmidt, T. J., Iridium Oxide for the Oxygen Evolution Reaction: Correlation between Particle Size, Morphology, and the Surface Hydroxo Layer from Operando XAS. *Chem. Mater.* **2016**, *28* (18), 6591-6604.

- 61. Nong, H. N.; Oh, H.-S.; Reier, T.; Willinger, E.; Willinger, M.-G.; Petkov, V.; Teschner, D.; Strasser, P., Oxide-Supported IrNiO_x Core—Shell Particles as Efficient, Cost-Effective, and Stable Catalysts for Electrochemical Water Splitting. *Angew. Chem. Int.* **2015**, *54* (10), 2975-2979.
- 62. Spori, C.; Briois, P.; Nong, H. N.; Reier, T.; Billard, A.; Kuhl, S.; Teschner, D.; Strasser, P., Experimental Activity Descriptors for Iridium-Based Catalysts for the Electrochemical Oxygen Evolution Reaction (OER). *ACS Catal.* **2019**, *9* (8), 6653-6663.
- 63. Shinagawa, T.; Garcia-Esparza, A. T.; Takanabe, K., Insight on Tafel Slopes from a Microkinetic Analysis of Aqueous Electrocatalysis for Energy Conversion. *Sci Rep* **2015**, *5*, 21.
- 64. Exner, K. S.; Sohrabnejad-Eskan, I.; Over, H., A Universal Approach To Determine the Free Energy Diagram of an Electrocatalytic Reaction. *Acs Catalysis* **2018**, *8* (3), 1864-1879.
- 65. Voiry, D.; Chhowalla, M.; Gogotsi, Y.; Kotov, N. A.; Li, Y.; Penner, R. M.; Schaak, R. E.; Weiss, P. S., Best Practices for Reporting Electrocatalytic Performance of Nanomaterials. *ACS Nano* **2018**, *12* (10), 9635-9638.
- 66. Guidelli, R.; Compton, R. G.; Feliu, J. M.; Gileadi, E.; Lipkowski, J.; Schmickler, W.; Trasatti, S., Defining the transfer coefficient in electrochemistry: An assessment (IUPAC Technical Report). *Pure and Applied Chemistry* **2014**, *86* (2), 245-258.
- 67. Guidelli, R.; Compton, R. G.; Feliu, J. M.; Gileadi, E.; Lipkowski, J.; Schmickler, W.; Trasatti, S., Definition of the transfer coefficient in electrochemistry (IUPAC Recommendations 2014). *Pure and Applied Chemistry* **2014**, *86* (2), 259-262.
- 68. Conway, B. E.; Tessier, D. F.; Wilkinson, D. P., Temperature Dependance of the Tafel Slope and Electrochemcial Barrier Symmetry Factor, Beta, in Electrode Kinetics. *J. Electrochem. Soc.* **1989**, *136* (9), 2486-2493.
- 69. Guidelli, R.; Compton, R. G.; Feliu, J. M.; Gileadi, E.; Lipkowski, J.; Schmickler, W.; Trasatti, S., Defining the transfer coefficient in electrochemistry: An assessment (IUPAC Technical Report). *Pure Appl. Chem.* **2014**, *86* (2), 245-258.
- 70. Castelli, P.; Trasatti, S.; Pollak, F. H.; Ogrady, W. E., SINGLE-CRYSTALS AS MODEL ELECTROCATALYSTS OXYGEN EVOLUTION ON RUO2 (110). *Journal of Electroanalytical Chemistry* **1986**, *210* (1), 189-194.
- 71. Fang, Y. H.; Liu, Z. P., Mechanism and Tafel Lines of Electro-Oxidation of Water to Oxygen on RuO2(110). *Journal of the American Chemical Society* **2010**, *132* (51), 18214-18222.
- 72. Zhang, R. G.; Pearce, P. E.; Duan, Y.; Dubouis, N.; Marchandier, T.; Grimaud, A., Importance of Water Structure and Catalyst-Electrolyte Interface on the Design of Water Splitting Catalysts. *Chemistry of Materials* **2019**, *31* (20), 8248-8259.
- 73. Liu, X.; Li, B.; Soto, F. A.; Li, X.; Unocic, R. R.; Balbuena, P. B.; Harutyunyan, A. R.; Hone, J.; Esposito, D. V., Enhancing Hydrogen Evolution Activity of Monolayer Molybdenum Disulfide via a Molecular Proton Mediator. *ACS Catalysis* **2021**, *11* (19), 12159-12169.
- 74. Klyukin, K.; Zagalskaya, A.; Alexandrov, V., Role of Dissolution Intermediates in Promoting Oxygen Evolution Reaction at RuO2(110) Surface. *The Journal of Physical Chemistry C* **2019**, *123* (36), 22151-22157.